New Journal of Physics
The open access journal for physics

Quasiparticle representation of coherent nonlinear optical signals of multi-excitons

Oleksiy Roslyak[1,2], Benjamin P Fingerhut[2], Kochise Bennett[2] and Shaul Mukamel[2]

[1] Theoretical Division of Los Alamos National Laboratory, Los Alamos, NM 87545, USA
[2] Chemistry Department, University of California, Irvine, CA 92697-2025, USA
E-mail: avroslyak@lanl.gov, bfingerh@uci.edu, kcbennet@uci.edu and smukamel@uci.edu

New Journal of Physics **15** (2013) 083049 (43pp)
Received 7 May 2013
Published 27 August 2013
Online at http://www.njp.org/
doi:10.1088/1367-2630/15/8/083049

Abstract. Multi-exciton Green's functions and scattering matrices in many-fermion systems are calculated using a quasiparticle approach based on a generalized Bethe–Salpeter equation. The simulation protocol only requires numerical diagonalization of the single-exciton manifold. Using coboson algebra all many-body effects are recast in terms of two tetradic exciton–exciton interactions: direct Coulomb scattering and Pauli exchange. The tedious equations-of-motion derivations and calculations of multi-exciton manifolds are avoided. The approach is applied to calculate the third- and fifth-order signals generated by sequences of femtosecond optical pulses. Several coherent fifth order optical signals that directly probe three-exciton states and their projections on double and single-exciton states are predicted.

Contents

1. Introduction 2
2. The coboson representation of multi-excitons 4
3. Green's functions and scattering matrices of cobosons 9
4. Probing the two-exciton manifold by third-order signals 12
5. Probing the three-exciton manifold by fifth-order signals 15
6. Numerical examples and discussion 22
7. Concluding remarks 25
Acknowledgments 26
Appendix A. Coboson algebra 27
Appendix B. The two-exciton Green's function and the scattering matrix 28
Appendix C. The three-excitons Green's function 29
Appendix D. Algorithm for computing the fifth-order techniques 31
Appendix E. Derivation of the third- and fifth-order time-domain response functions 33
Appendix F. Sum-over-states expressions for the third-order impulsive response 39
Appendix G. Third-order signals with exciton transport 41
References 42

1. Introduction

Elementary excitations of many-fermion systems can be described as quasiparticles (QP) and are viewed as independent harmonic oscillators. The quasiparticle approach is widely used in the calculation of transport and optical properties of metals, semiconductors and strongly correlated quantum materials [1]. Examples include the Landau theory of metals, the Drude model, plasmons, magnons, etc [2–4]. Much effort has focused on the dispersion of single QP by utilizing a mean-field formalism such as the semiconductor Bloch equations [5]. Inherently, this level of theory only takes into account two-point, Coulomb-induced correlations between interacting particles. In smaller systems, such as quantum wells and dots, the interacting particles become 'strongly correlated' and interactions between them may no longer be treated as local scattering events [6]. Various nonlinear optical techniques can however create and manipulate a controlled number of QP [11, 12] whose interactions are mapped into effective anharmonicities [13] and provide an interesting window into the many-body physics. These techniques are sensitive to multi-point correlations. Sequences of ultrafast optical pulses can be designed such that the signals vanish for non-interacting QP, thus providing a background-free probe for anharmonic deviations from the independent particle picture. Four and six wave mixing techniques probe four- and six-point correlations respectively [6–10].

We propose a Green's function approach based on composite boson (coboson) algebra [22] for calculating such correlations and apply it onwards the study of two- and three-exciton states. The boson picture is attractive since it provides a convenient computational tool and a simple, physical, almost classical, picture of weak excitations that is exact in the linear response regime. The boson description gradually breaks down as the excitation level

is increased and the response becomes nonlinear. Considerable effort has been devoted to developing various bosonization schemes which go beyond the linear response regime by transforming the original fermion degrees of freedom into weakly interacting bosons. These schemes attempt to treat higher levels of excitations by lumping all interactions into an effective 'direct' Coulomb scattering [14]. However, they cannot fully describe Pauli-driven exciton exchange by an effective Hermitian Hamiltonian. A proper many-body treatment requires various adjustments to the bosonization approaches. Several approaches treated the problem to first order in quasiparticle density by an effective scattering between two boson-excitons. For semiconductors, Hanamura and co-workers [15, 16] employed the Usui transformation, which uses a non-Hermitian Hamiltonian, to calculate the nonlinear response. The boson commutation relations were q-deformed [17]. This theory was adopted in quantum optics to describe Dicke super-radiance. The Jordan–Wigner approach to Pauli exchange transforms the Pauli excitations in one-dimensional systems to non- or weakly interacting fermions [24]. This method has been successfully applied to J-aggregates [25]. Another example of such deformation was adopted by Mukamel and co-workers [18, 19] for the Frenkel excitons and by Knoester *et al* for hard-core bosons [20]. Combescot and Betbeder-Matibet [21, 22] developed a coboson formalism that works for higher quasiparticle densities. This requires an infinite expansion of both the Hamiltonian and commutation relations in coboson operators. The coboson algebra can be formulated in compact form by introducing two quantities: an exciton scattering operator V and an operator D representing the deviation from bosonicity. It is not necessary to derive the exact Hamiltonian in the coboson form in order to calculate various physical observables [23].

This paper focuses on developing a Green's function approach for the nonlinear optical response and identifying signatures of multiple excitons in multidimensional signals. Two protocols based either on sum-over-states (SOS) or QP are primarily used to calculate the nonlinear optical responses. Both start with interacting many-fermion systems whose ground state $|g\rangle$ is given by a single Slater determinant which can be obtained at the Hartree–Fock or DFT level. The block-diagonal Hamiltonian is assumed to conserve the number of excitons (i.e. the off-diagonal blocks vanish). This Heitler–London approximation for Frenkel excitons is the only approximation on the Coulomb interaction that we will make. It is expected to hold for typical molecules and semiconductors. We consider the following Hamiltonian blocks: a single, non-degenerate ground state, N single electron–hole pair states, $\frac{N(N-1)}{2}$ two electron–hole pairs, etc. The n-pair blocks has C_N^n states, with N being the system size. In the SOS formalism the relevant blocks are diagonalized to yield multi-exciton states [18]. The nonlinear optical response is then recast in terms of multi-exciton Green's functions and transition dipole elements between the multi-exciton states. This protocol has several drawbacks since the multi-exciton wavefunctions contain much more information than needed for typical observables. The numerical effort grows rapidly with the number of excitations. Moreover, massive cancellation of $\sim N^2$ scaling terms in various pathways to yield final $\sim N$ signals complicates the calculation and analysis [26].

The QP approach mitigates these difficulties. A QP description has been developed earlier based on nonlinear exciton equations (NEE) [19, 27], also known as dynamics controlled truncation approach [6]. In this picture, Pauli exclusion is exactly accounted for by the deformation of boson commutators. Products of uncorrelated electron/hole pairs are used as a basis set for multiple excitations. The nonlinear response originates from the scattering matrix ($\Gamma^{(n)}$), defined via the Bethe–Salpeter equation, which uses n quasiparticle boson Green's functions $G^{(n,0)}$ as a reference. Calculating the scattering matrix requires only simple algebraic

manipulations (products and inversions of matrices); expensive matrix diagonalizations are not necessary. The order-by-order derivation of the NEEs is the bottleneck which so far had prevented its application to more than two interacting excitons. For example, in order to find $\Gamma^{(3)}$ for the third-order response, one needs to solve C_N^1 single-exciton equations coupled to C_N^2, C_N^3 equations for double- and triple-excitons respectively.

By treating the excitons as coboson QP we can calculate high-order ($\chi^{(5)}$ and above) nonlinear optical responses. Our QP approach relies solely on the coboson algebra without resorting to equations of motion (NEE) or numerical multi-exciton diagonalization as in the SOS [18]. The required parameters for this algebra require knowledge of the two-exciton Hamiltonian block only. Explicit forms of the three-exciton and higher blocks are not needed. Several nonlinear, high-order optical techniques in the coboson representation will be derived by using loop diagrams. All necessary ingredients, such as boson Green's functions, coboson scattering matrices and transition dipole moments, will be directly obtained from the coboson algebra.

We shall further address some difficulties in recasting the SOS formalism in the coboson basis. In particular we shall focus on those arising from over-completeness of the two coboson manifold (N^2 size and with some unphysical states, compared with $N(N-1)/2$ true two-exciton space). The multi-exciton Hamiltonian blocks become singular in this representation. Enlarging the system size results in a singular part of the Hamiltonian, known as the self energy. Usually, in semiconductors, such effects are attributed to the system size reduction. The formalism may be extended to solve more complex models, e.g. by adding coupling to phonons. This will be done in appendix G by proper averaging of products of Green's functions.

2. The coboson representation of multi-excitons

The coboson algebra is the key element for our approach. It is instructive to derive its elements starting with the many-body Hamiltonian of a system of interacting fermions. These fermions are electrons at discrete position $m1$ created from the ground state $c_{m1}^{\dagger}|g\rangle$ and holes at position $m2$ created via $d_{m2}^{\dagger}|g\rangle$. The respective creation/annihilation operators obey the fermionic anti-commutation rules: $\{c_{m1}, c_{n2}^{\dagger}\} = \{d_{m1}, d_{n2}^{\dagger}\} = \delta_{m1,n2}$. We use the notation of [18] whereby subscripts in the form of letter+number define the electron and hole indices. For a collection of N two level chromophores those indices run over their positions and neglect spins. We adopt the tight-binding Hamiltonian in Heitler–London approximation to describe elementary excitations [19]. It is given by the sum of the single particle contribution H_0, the Coulomb interaction H_{C} and the dipole coupling with the radiation field H_{I}:

$$H = H_0 + H_{\mathrm{C}} + H_{\mathrm{I}}, \tag{1}$$

$$H_0 = \sum_{m1,n1} t_{m1,n1}^{(1)} c_{m1}^{\dagger} c_{n1} + \sum_{m2,n2} t_{m2,n2}^{(2)} d_{m2}^{\dagger} d_{n2}, \tag{2}$$

$$H_{\mathrm{C}} = \frac{1}{2} \sum_{m1,n1,k1,l1} V_{m1n1,k1l1}^{(1)} c_{m1}^{\dagger} c_{n1}^{\dagger} c_{k1} c_{l1} + \frac{1}{2} \sum_{l2,k2,n2,m2} V_{m2n2,k2l2}^{(2)} d_{m2}^{\dagger} d_{n2}^{\dagger} d_{k2} d_{l2} - \sum_{m1,n2,k2,l1} W_{m1n2,l2k1}^{(1,2)} c_{m1}^{\dagger} d_{n2}^{\dagger} d_{l2} c_{k1}, \tag{3}$$

$$H_{\rm I} = -\sum_{m1,m2} E^{+}(t)\mu^{\star}_{m1,m2}c^{\dagger}_{m1}d^{\dagger}_{m2} + E^{-}(t)\mu_{m1,m2}d_{m2}c_{m1}. \tag{4}$$

Here the matrices $\mathbf{t}$ describe the hopping between the sites. The tetradic matrices $\mathbf{V}^{(1)}$, $\mathbf{V}^{(2)}$ describe electron/electron and hole/hole Coulomb repulsion, while $\mathbf{W}^{(1,2)}$ represent electron–hole attraction. Equation (4) represents the interaction with right/left components of the optical field $E^{\pm}(t)$ via transition dipole moments matrix $\boldsymbol{\mu}$. Hereafter matrices are denoted by bold letters.

To develop the QP picture for electronic excitations we shall switch from the above fermion picture to uncorrelated electron/hole pairs and eventually to the coboson QP picture. In order to transform the fermion Hamiltonian to the uncorrelated electron–hole representation, we first note that the matter Hamiltonian (equations (2) and (3)) conserves the number of excitations (electron–hole pairs). It is therefore possible to focus on one subspace of n-exciton states and construct a electron/hole pair Hamiltonian that coincides with the original fermion Hamiltonian in that space. Below we only consider the single $|\psi^{x}\rangle = B^{\dagger}_{n}|g\rangle$ and two-exciton $|\psi^{xx}\rangle = B^{\dagger}_{m}B^{\dagger}_{n}|g\rangle$ spaces, but the method can be extended to higher spaces. The respective electron/hole pair creation operator is given by $B^{\dagger}_{m} \equiv c^{\dagger}_{m1}d^{\dagger}_{m2}$, with the subscript m standing for the pair $m = m1, m2$ in the site basis. When $m1 = m2$ it creates the Frenkel exciton and the charge transfer state otherwise. It is worth noting that physical excitons form a subspace of electron/hole pairs obtained by imposing Pauli constraints on the over-complete electron/hole pair basis. For the double excitations, the constraints assume $m > n$ form, thus reducing the size of $|\psi^{xx}\rangle$ from N^2 to $N(N-1)/2$. After some algebra, the resulting electron–hole pair Hamiltonian assumes the from [18, 25]

$$H = H_1 + H_2 + H_{\rm I}, \tag{5}$$

$$H_1 + H_2 = \sum_{m,n} h_{m,n}B^{\dagger}_{m}B_{n} + \sum_{m,n,k,l} U_{lk,nm}B^{\dagger}_{m}B^{\dagger}_{n}B_{k}B_{l}, \tag{6}$$

$$h_{m,n} = t^{(1)}_{m1,n1}\delta_{m2,n2} + t^{(2)}_{m2,n2}\delta_{m1,n1} - W^{(1,2)}_{n2n1,m2m1}, \tag{7}$$

$$U_{lk,nm} = U^{(1)}_{lk,nm} + U^{(2)}_{lk,nm}, \tag{8}$$

$$\begin{aligned} U^{(1)}_{lk,nm} &= -\tfrac{1}{4}\left(h_{m,k}\delta_{n,l} + h_{n,l}\delta_{m,k}\right), \\ U^{(2)}_{lk,nm} &= \tfrac{1}{4}\Big(V^{(1)}_{l1k1,n1m1}\delta_{m2,k2}\delta_{n2,l2} + V^{(2)}_{l2k2,n2m2}\delta_{m1,k1}\delta_{n1,l1} \\ &\quad - W^{(1,2)}_{k2k1,m2m1}\delta_{n1,l1}\delta_{n2,l2} - W^{(1,2)}_{l2l1,n2n1}\delta_{m1,k1}\delta_{m2,k2}\Big), \end{aligned} \tag{9}$$

$$H_{\rm I} = -\sum_{m} E^{+}(t)\mu^{\star}_{m}B^{\dagger}_{m} + E^{-}(t)\mu_{m}B_{m}. \tag{10}$$

The above Hamiltonian is block-diagonal in the basis $|\psi^x\rangle$, $|\psi^{xx}\rangle$ and conserves the number of excitations. To recast the Hamiltonian (equation (6)) in the coboson representation, we first diagonalize the single-particle block H_1 and obtain the single-exciton states $|1\rangle$ and energies E_1:

$$\begin{aligned} &H_1|1\rangle = E_1|1\rangle, \\ &\langle 2|1\rangle = \delta_{1,2}, \end{aligned} \tag{11}$$

where we label the single-exciton states in increasing order of energy (i.e. $|1\rangle$, $|2\rangle$, etc). This allows one to formally introduce the coboson creation operators by projecting the uncorrelated electron/hole pair $|m\rangle$ onto the single coboson states $|1\rangle$. Back and forth transformations between the cobosons (excitons) and the electron–hole pairs are given by

$$\begin{aligned} B_1^\dagger &= \sum_m B_m^\dagger \langle m|1\rangle, \\ B_m^\dagger &= \sum_1 B_1^\dagger \langle 1|m\rangle, \\ B_1^\dagger|g\rangle &= |1\rangle. \end{aligned} \tag{12}$$

We shall adopt the following notation for subscripts: letter subscripts $B_\nu^\dagger$ ($\nu = k, l, m, n$, etc) are reserved for the original electron/hole pair basis while numerical subscripts $B_j^\dagger$ ($j = 1, 2, 3$, etc) are used for the cobosn basis. The coboson basis for the electron/hole pairs is over-complete, yielding the multi-coboson states: $|\ldots, 2, 1\rangle = \ldots B_2^\dagger B_1^\dagger|g\rangle$. Observable multi-exciton states are obtained via projection technique used in appendix F in order to recover the SOS block-diagonal Hamiltonian (figure 1).

The basic elements of the coboson algebra were developed in [36] and summarized in appendix A. These are: Pauli scattering (A.1), direct Coulomb scattering (A.4) and the interaction expansion (A.11). The over-completeness of the coboson basis results in a specific form of the identity operator (A.9). The algebra is fully described by two types of coboson–coboson interactions given by tetradic matrices: Pauli exchange $\boldsymbol{\lambda}$ and the Coulomb scattering $\boldsymbol{\xi}$. These carry all many-body information necessary for computing the many-exciton Green's functions and can be graphically visualized by Shiva diagrams which allow for rapid calculations and interpretation of their products and combinations [22]. These interactions can be obtained by direct comparison of the Hamiltonian and commutator relations for the cobosons with those for the uncorrelated particle bosonized Hamiltonian as described below.

Based *solely* on the algebraic rules, the two-exciton block of the Hamiltonian assumes the form [22]

$$\begin{aligned} &H = H_1 + H_2 + H_I(B_1^\dagger, B_1), \\ &H_1 + H_2 = \sum_1 E_1 B_1^\dagger B_1 + \sum_{1,2,3,4} \frac{1}{4}(-(E_1 + E_2)\delta_{3,1}\delta_{4,2} + \xi_{12,34}) B_3^\dagger B_4^\dagger B_2 B_1. \end{aligned} \tag{13}$$

By comparing the single-particle blocks H_1 of the coboson (equation (13)) and electron–hole pair (equation (6)) Hamiltonians, we obtain

$$\sum_1 E_1 \langle m|1\rangle\langle 1|n\rangle = h_{m,n}. \tag{14}$$

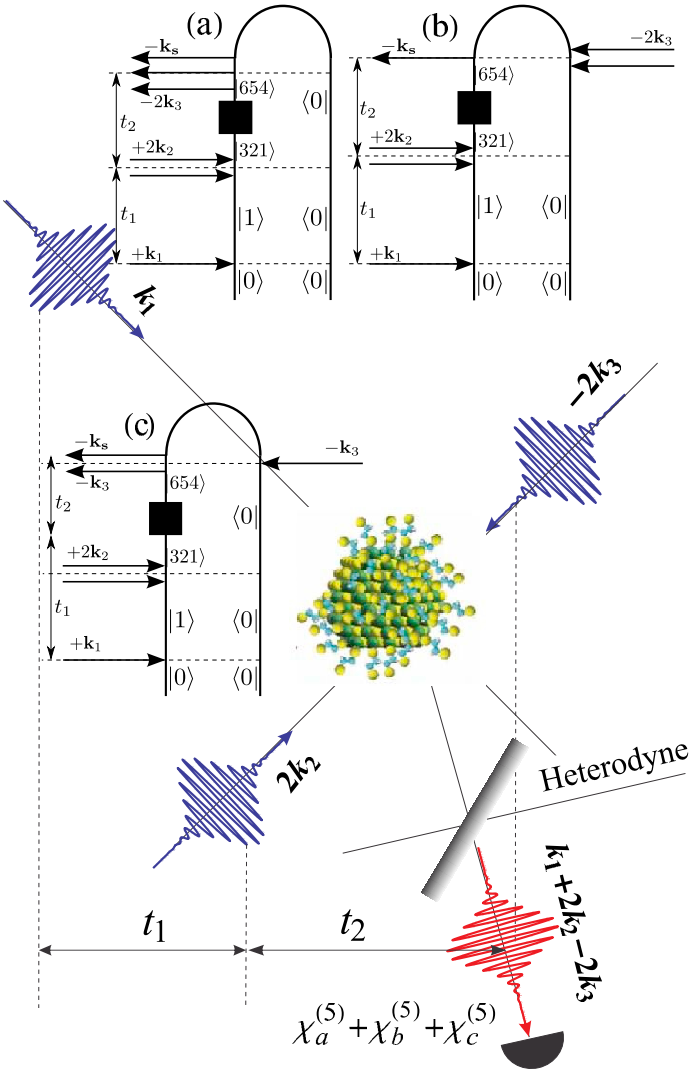

Figure 1. Probing triple quantum coherence by a fifth-order technique.

By utilizing equations (14) and (12) in conjunction with equation (13), we find

$$-\sum_{1,2,3,4}\frac{1}{4}\left(E_1+E_2\right)\delta_{3,1}\delta_{4,2}B_3^\dagger B_4^\dagger B_2 B_1=\sum_{m,n,k,l}\frac{1}{4}U^{(1)}_{lk,nm}B_m^\dagger B_n^\dagger B_k B_l. \tag{15}$$

The remaining terms in H_2 of equations (13) and (14) can be projected onto the two coboson basis. This constitutes one of our main results—the direct Coulomb scattering matrix is given by the double pair Coulomb coupling matrix projected onto the two-coboson subspace:

$$\xi_{12,34}=\sum_{m,n,k,l}U^{(2)}_{lk,nm}\langle 3|m\rangle\langle 4|n\rangle\langle k|2\rangle\langle l|1\rangle, \tag{16}$$

where we have used the orthogonality relation $\sum_l\langle 1|l\rangle\langle l|1'\rangle=\delta_{1,1'}$. The Shiva diagrams corresponding to equation (16) are depicted in figure 2(a). Equation (13) reduces to the Hubbard

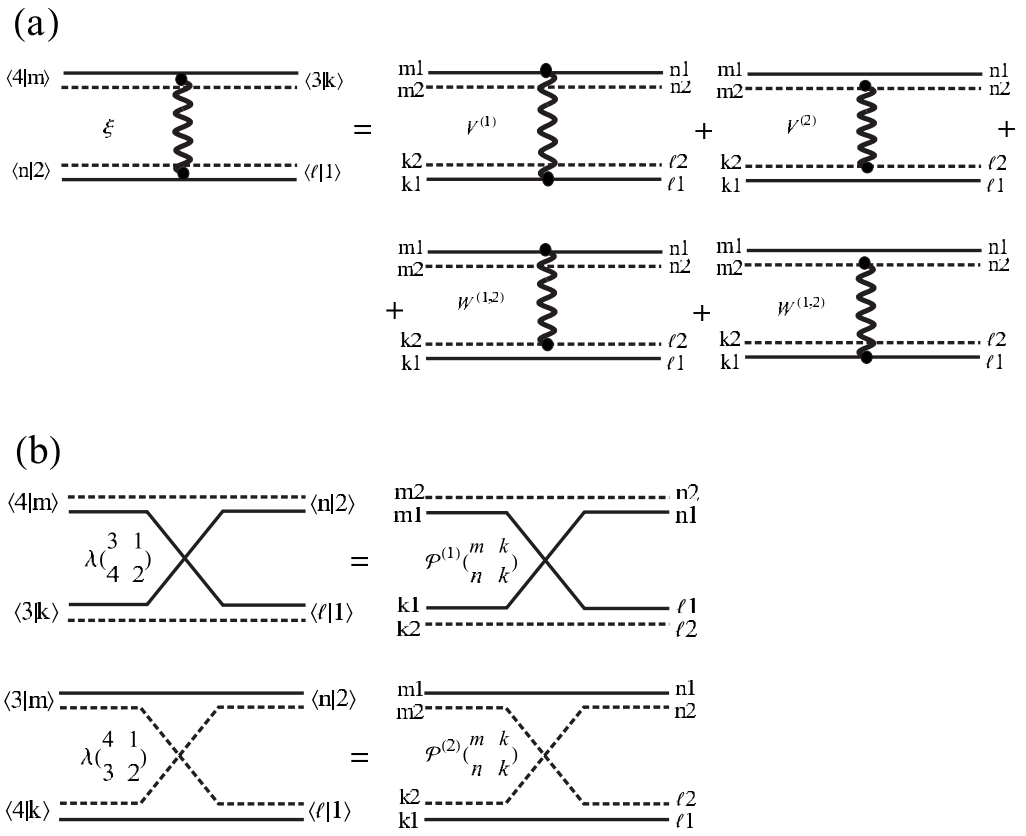

Figure 2. Shiva diagrams. Panel (a) is for direct Coulomb scattering (equation (16)). Panel (b) is for Pauli exchange (equation (19)). Rules of diagrams: (1) solid lines—electrons, dashed lines—holes. Solid lines correspond to δ functions, wiggly lines are the connectors of V and W type.

model if all Coulomb interactions occur only on-site and the indices m run not only on the positions but also on spin variables (in which case matrix $\boldsymbol{\xi}$ vanishes).

From the actions of the commutators in equations (A.4) and (A.10) on the single electron/hole pair we obtain

$$[B_4,\, B_2^{\dagger}]|\psi^{(x)}\rangle = \left(\delta_{4,2} - \sum_{1,3} \left(\lambda_{21,43} + \lambda_{21,34}\right) B_3^{\dagger} B_1\right) |\psi^{(x)}\rangle, \tag{17}$$

$$\left[B_m,\, B_n^{\dagger}\right] |\psi^{(x)}\rangle = \left(\delta_{m,n} - \sum_{k,l} \mathcal{P}_{lk,nm} B_k^{\dagger} B_l\right) |\psi^{(x)}\rangle. \tag{18}$$

Using equation (12) and the orthogonality relations, we obtain the Pauli exchange matrix elements:

$$\lambda_{21,43} = \sum_{m,n,k,l} \delta_{m1,l1}\delta_{n1,k1}\delta_{m2,n2}\delta_{k2,l2}\langle 3|k\rangle\langle 4|m\rangle\langle n|2\rangle\langle l|1\rangle$$

$$= \sum_{n,l} \langle 3|n1, l2\rangle\langle 4|l1, n2\rangle\langle n1, n2|2\rangle\langle l1, l2|1\rangle. \tag{19}$$

Corresponding Shiva diagrams are shown in figure 2(b). The dipole coupling is obtained by transforming equation (4):

$$H_{\mathrm{I}} = \sum_{1} E^{+}(t)\mu_1^{\star} B_1^{\dagger} + E^{-}(t)\mu_1 B_1,$$
$$\mu_1^{\star} = \sum_{m} \mu_m^{\star} \langle 1|m\rangle. \tag{20}$$

In summary, the required coboson algebra parameters were calculated by projecting the system Hamiltonian in the fermion representation onto the uncorrelated electron–hole pair and coboson representations and then comparing the two. Our starting point was the fermionic Hamiltonian which describes any number of excitations in the system. We then derived the Hamiltonian in the electron–hole pair representation by truncating the fermion Hamiltonian to include up to two excitations in the system. The coboson form of the Hamiltonian was obtained by using the corresponding algebraic rules. By comparing the electron–hole pair and coboson representations, we expressed the $\boldsymbol{\xi}$ matrix of the coboson algebra in terms of $\mathbf{U}$ matrix of the electron–hole pair representation, which in turn was written in terms of the Coulomb matrix elements of the original electron/hole Hamiltonian. The energies/eigenfunctions of the single-exciton manifold were obtained by comparing of the action of the electron–hole pair Hamiltonian acting on this manifold. Finally, we expressed the $\boldsymbol{\lambda}$ matrix of the coboson algebra in terms of the electron–hole exchange $\mathcal{P}$ matrix. This was accomplished by comparing the action of the commutator in both pictures on the single-exciton manifold using the coboson and the fermion operators.

3. Green's functions and scattering matrices of cobosons

We next turn to calculating the Green's functions and exciton scattering matrices. The Green's function matrix elements in the frequency domain are defined by

$$G^{(n)}_{2n\ldots n+1,n\ldots 1}(\omega) = \langle g|B_{2n}\ldots B_{n+1}\frac{1}{\omega - H + \mathrm{i}\eta}B_n^{\dagger}\ldots B_1^{\dagger}|g\rangle \tag{21}$$

with $\eta \to 0^{+}$. The main advantage of the coboson over the SOS formalism is that the expensive diagonalizations of multi-exciton blocks of H are not necessary for calculation of the Green's functions $\mathbf{G}^{(n)}$. In order to describe the coboson scattering, we start with the Bethe–Salpeter equation which describes the deviation of the cobosons from free bosons:

$$\mathbf{G}^{(n)} = \mathbf{G}^{(n,0)}\boldsymbol{\Delta}^{(n)} + \mathbf{G}^{(n,0)}\boldsymbol{\Gamma}^{(n)}\mathbf{G}^{(n,0)}. \tag{22}$$

Here $\mathbf{G}^{(n,0)}$ is free-boson zero-order Green's function matrix. It is obtained by treating the excitons as structureless ($\boldsymbol{\lambda} \to 0$) and non-interacting ($\boldsymbol{\xi} \to 0$) bosons:

$$G^{(n,0)}_{2n\ldots n+1,n\ldots 1} = I_{2n\ldots n+1,n\ldots 1}\Big/\left(\omega - \sum_{j=1}^{n} E_n\right), \tag{23}$$

where elements of the identity matrix $\mathbf{I}$ are equal to one for the diagonal elements and zero otherwise. The $2n$-adic matrix $\boldsymbol{\Delta}^{(n)}$ is given by

$$\Delta^{(2)}_{12,34} = \delta_{4,2}\delta_{3,1} + \delta_{3,2}\delta_{4,1}, \tag{24}$$

$$\Delta^{(3)}_{123,456} \equiv \delta_{4,1}\delta_{5,2}\delta_{6,3} + \delta_{4,1}\delta_{5,3}\delta_{6,2} + \delta_{4,2}\delta_{5,1}\delta_{6,3} + \delta_{4,2}\delta_{5,3}\delta_{6,1} + \delta_{4,3}\delta_{5,1}\delta_{6,2} + \delta_{4,3}\delta_{5,2}\delta_{6,1} \tag{25}$$

permutes the energies in equation (23) and does not change the bosonic nature of $\mathbf{G}^{(2,0)}$. It is introduced for consistency with the modified Dyson equation derived below. $\mathbf{\Gamma}^{(n)}$ is the coboson scattering matrix yet to be determined.

Utilizing the coboson algebra rules, we can move $\frac{1}{\omega - H + \mathrm{i}\eta}$ in the multi-coboson Green's function (21) to the right until it eventually acts on the ground state. This will generate the Coulomb terms from the exciton scattering operator V and the Pauli blocking via the operator D. This procedure leads to the generalized Dyson equation

$$\mathbf{G}^{(n)} = \mathbf{G}^{(n,0)}\left(\mathbf{\Delta}^{(n)} - \mathbf{\Lambda}^{(n)}\right) + \mathbf{G}^{(n,0)}\,\mathbf{\Xi}^{(n)}\mathbf{G}^{(n)}, \tag{26}$$

where $\mathbf{\Xi}^{(n)}$ and $\mathbf{\Lambda}^{(n)}$ are known functions of the Coulomb direct interaction $\boldsymbol{\xi}$ and exciton exchange $\boldsymbol{\lambda}$. $\mathbf{\Lambda}^{(n)}$ accounts for Fermi statistics, which are not included in the ordinary Dyson equation. The matrix $\mathbf{\Delta}^{(n)}$ makes sure that bosons of the same energy are indistinguishable. In appendix B, we worked out the details for the two coboson case ($n = 2$):

$$\Lambda^{(2)}_{12,34} = \lambda_{21,43} + \lambda_{21,34,} \tag{27}$$

$$\Xi^{(2)}_{12,34} = \xi_{21,43}.$$

Similarly, the case of three-coboson interactions ($n = 3$) was obtained in appendix C:

$$\mathbf{\Lambda}^{(3)} = \tilde{\mathbf{\Lambda}}^{(3)} - 2\boldsymbol{\xi}^{(3,1)}(\mathbf{I} - \mathbf{G}^{(3,0)}\boldsymbol{\xi}^{(3,1)})^{-1}\mathbf{G}^{(3,0)}(\mathbf{\Delta}^{(3)} - \tilde{\mathbf{\Lambda}}^{(3)}), \tag{28}$$

$$\mathbf{\Xi}^{(3)} = \tilde{\boldsymbol{\xi}}^{(3,1)} + \tilde{\boldsymbol{\xi}}^{(3,2)} + \tilde{\boldsymbol{\xi}}^{(3,3)}, \tag{29}$$

where we have introduced several auxiliary quantities denoted by tildes:

$$\tilde{\Lambda}^{(3)}_{123,456} = \tilde{\lambda}^{(0)}_{123,456} - \tilde{\lambda}^{(1)}_{123,456}, \tag{30}$$

$$\begin{aligned}
-\tilde{\lambda}^{(0)}_{123,456} &= -\delta_{4,1}\left(\lambda_{32,65} + \lambda_{32,56}\right) - \delta_{4,2}\left(\lambda_{31,65} + \lambda_{31,56}\right) - \delta_{4,3}\left(\lambda_{21,65} + \lambda_{21,56}\right) \\
&-\delta_{5,1}\left(\lambda_{32,46} + \lambda_{32,64}\right) - \delta_{5,2}\left(\lambda_{31,46} + \lambda_{31,64}\right) - \delta_{5,3}\left(\lambda_{21,46} + \lambda_{21,64}\right) \\
&-\delta_{6,1}\left(\lambda_{32,45} + \lambda_{32,54}\right) - \delta_{6,2}\left(\lambda_{31,45} + \lambda_{31,54}\right) - \delta_{6,3}\left(\lambda_{21,45} + \lambda_{21,54}\right) \\
\tilde{\lambda}^{(1)}_{123,456} &= \sum_{3'}\left(\lambda_{21,43'} + \lambda_{21,3'4}\right)\left(\lambda_{33',65} + \lambda_{33',56}\right) + \sum_{3'}\left(\lambda_{31,43'} + \lambda_{31,3'4}\right)\left(\lambda_{23',65} + \lambda_{23',56}\right) \\
&+ \sum_{3'}\left(\lambda_{32,43'} + \lambda_{32,3'4}\right)\left(\lambda_{3'1,65} + \lambda_{3'1,56}\right),
\end{aligned} \tag{31}$$

$$\begin{aligned}
\tilde{\xi}^{(3,1)}_{321,3'2'1'} &= \xi_{21,2'1'}\delta_{3,3'}, \\
\tilde{\xi}^{(3,2)}_{321,3'2'1'} &= \xi_{31,2'1'}\delta_{2,3'}, \\
\tilde{\xi}^{(3,3)}_{321,3'2'1'} &= \xi_{22,2'1'}\delta_{1,3'}.
\end{aligned} \tag{32}$$

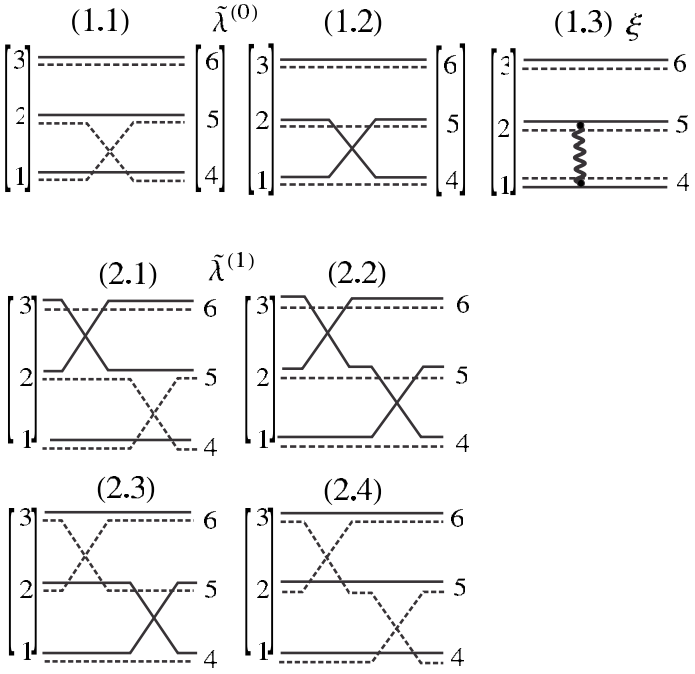

Figure 3. Shiva diagrams for three-exciton scattering. Panels (1, 2) two/three-particle interactions: Coulomb in equation (C.7) and Pauli in equation (C.3).

Their physical significance is best described by the Shiva diagrams in figure 3 and is further discussed in appendix C.

Note that all $\mathbf{A}^{(n)}$ quantities are tensors of rank $2n$. They may be mapped onto the regular matrices (rank 2) of $\mathbf{A}_{N^n,N^n}$ size, as described in appendix A. Comparing the modified Dyson (equation (26)) with the Bethe–Salpeter equation (22) in their matrix form and carrying out some straightforward algebra (see appendix B) yields the exciton scattering matrix

$$\mathbf{\Gamma}^{(n)} = (\mathbf{I} - \mathbf{\Xi}^{(n)}\mathbf{G}^{(n,0)})^{-1}\mathbf{\Xi}^{(n)}\mathbf{G}^{(n,0)}(\mathbf{I} - \mathbf{\Lambda}^{(n)})(\mathbf{G}^{(n,0)})^{-1} - \mathbf{\Lambda}^{(n)}(\mathbf{G}^{(n,0)})^{-1}. \quad (33)$$

$\mathbf{\Gamma}^{(n)}$ can be mapped back onto the rank $2n$ tensor and is one of the key quantities of this paper.

In the coming sections, we shall apply these Green's functions and scattering matrices to calculate nonlinear optical response functions. Our protocol consists of the following steps:

1. Starting with the many-fermion Hamiltonian, derive the effective Hamiltonian and the commutation rules in the coboson representation only for the two exciton manifold. This allows one to calculate the two elementary tetradic matrices: a two exciton Coulomb scattering matrix $\boldsymbol{\xi}$ and a Pauli exclusion matrix $\boldsymbol{\lambda}$. These are the only ingredients required for calculating the response functions to all orders.
2. Write down loop diagrams for the response function of interest and use them to construct Green's function expressions for the response.
3. Use the Bethe–Salpeter equation to eliminate the terms representing the harmonic boson nonlinear response, whose sum must vanish identically.

4. Calculate the necessary Green's functions and scattering matrices using algebraic properties of the coboson operators.
5. Insert the Green's functions in the expressions from step 3 and finally obtain the response.

These steps are simple and, even though step 4 requires the coboson algebra, it can be carried out with minimal effort. The coboson algebra may be used for recasting these signals in SOS form (see appendix F).

4. Probing the two-exciton manifold by third-order signals

We first consider a continuous-wave (CW), frequency-domain experiment in which the system is subjected to three stationary beams and calculate the signal with frequency $\omega_s = \omega_1 + \omega_2 - \omega_3$. This is the only third-order signal allowed by our dipole selection rules. The susceptibility, $\chi^{(3)}$, is represented by many diagrams (for diagram rules see appendix D.2). However, we know that the free-boson contributions must cancel out. Since the free-boson system is linear, we need only consider terms which contain two-exciton states. We are thus left with only the two diagrams given in figure 4. The susceptibility, which can be read off the diagrams, is

$$\chi^{(3)}(-\omega_s;\omega_1,\omega_2,-\omega_3) = \sum_{p\{\omega_i\}}\Big[\langle\hat{\mu}^-\hat{G}^{(1)}(\omega_1+\omega_2-\omega_3)\hat{\mu}^-\hat{G}^{(2,0)}(\omega_1+\omega_2)\hat{\Gamma}^{(2)}(\omega_1+\omega_2)\hat{G}^{(2,0)} \times(\omega_1+\omega_2)\hat{\mu}^+\hat{G}^{(1)}(\omega_1)\hat{\mu}^+\rangle - \langle\hat{\mu}^-\hat{G}^{(1),\dagger}(\omega_3)\hat{\mu}^-\hat{G}^{(2,0)} \times(\omega_1+\omega_2)\hat{\Gamma}^{(2)}(\omega_1+\omega_2)\hat{G}^{(2,0)}(\omega_1+\omega_2)\hat{\mu}^+\hat{G}^{(1)}(\omega_1)\hat{\mu}^+\rangle\Big], \tag{34}$$

where $\hat{G}$, $\hat{\Gamma}$ are the operators corresponding to the Green's functions (free-boson form) and the scattering matrix respectively; $\hat{\mu}^{\pm}$ are the raising/lowering part of the dipole moment operator. Since, in CW experiments, we do not have control over the time ordering of various interactions, we will have to permute the order of the three field frequencies ω_1, ω_2 and ω_3. $\sum_{p\{\omega_i\}}$ represents the summation over those 3! permutations. Expanding equation (34) in the one-exciton state basis yields our final compact expression for the third-order susceptibility

$$\chi^{(3)}(-\omega_s;\omega_1,\omega_2,-\omega_3) = \sum_{p\{\omega_i\}}\sum_{4,3,2,1}\mu_4\mu_3\mu_2^\star\mu_1^\star\mathcal{G}_1(\omega_1)\,\mathcal{G}_{21}(\omega_1+\omega_2) \times\Gamma^{(2)}_{21,43}(\omega_1+\omega_2)\mathcal{G}_{43}(\omega_1+\omega_2)\left[\mathcal{G}_4(\omega_1+\omega_2-\omega_3)-\mathcal{G}_4^\star(\omega_3)\right], \tag{35}$$

Here the dipole moments μ are given by equation (20). It is worth noting that the dipole moments above are of the free-boson model. Justification of this non-trivial fact is given in appendix E. The scattering matrix $\Gamma^{(2)}$ is given in equations (33), (27). Note that the indices of $\Gamma^{(2)}$ appear in the reverse order of their respective states along the loop; this follows from of our convention for identifying matrix elements of the Green's function (equation (B.1). We have further introduced the following abbreviated notation for the single-exciton free-boson Green's function:

$$\mathcal{G}_1(t) \equiv \langle 1|G^{(1)}(t)|1\rangle = -\mathrm{i}\theta(t)\,\mathrm{e}^{-\mathrm{i}(E_1-\mathrm{i}\gamma_1)}, \tag{36}$$

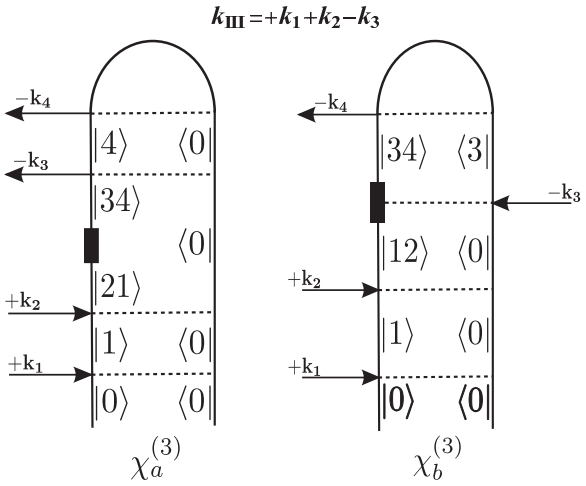

Figure 4. Loop diagrams for the third-order susceptibility. These diagrams are frequency domain counterparts to diagrams III_a and III_b that appear later in figure 6. The other two anharmonic diagrams, I_a and II_a, are both identical to III_b in the frequency domain because the order of interactions is not controlled. Equation (34) can be read directly off these diagrams.

$$\mathcal{G}_1^*(t) \equiv \langle 1|G^{(1)\dagger}(t)|1\rangle = \mathrm{i}\theta(t)\,\mathrm{e}^{\mathrm{i}(E_1+\mathrm{i}\gamma_1)}, \tag{37}$$

where γ_1 are the pure dephasing rates for the coboson states. In the frequency-domain, these become

$$\mathcal{G}_1(\omega) \equiv \int \mathrm{d}t\mathcal{G}_1(t)\,\mathrm{e}^{\mathrm{i}\omega t} = \frac{1}{\omega - E_1 + \mathrm{i}\gamma_1}. \tag{38}$$

We further introduce similar abbreviated notation for the frequency-domain free-boson Green's function for two and three excitons (the latter will be used in the next section):

$$\mathcal{G}_{21}(\omega) \equiv \langle 21|G^{(2,0)}|21\rangle = \frac{1}{\omega - E_2 - E_1 + \mathrm{i}\gamma_2 + \mathrm{i}\gamma_1}, \tag{39}$$

$$\mathcal{G}_{321}(\omega) \equiv \langle 321|G^{(3,0)}|321\rangle = \frac{1}{\omega - E_3 - E_2 - E_1 + \mathrm{i}\gamma_3 + \mathrm{i}\gamma_2 + \mathrm{i}\gamma_1}. \tag{40}$$

In these expressions, all Green's functions represent free-boson evolution in the relevant exciton-manifold as given by the number of indices; $\mathcal{G}_1$, $\mathcal{G}_{21}$ and $\mathcal{G}_{321}$ represent evolution in the single-, double- and triple-exciton manifolds respectively.

We next turn to time-domain techniques. We first consider an experiment in which the system is subjected to a sequence of three, temporally well-separated pulses with wave-vectors $\mathbf{k_1}$, $\mathbf{k_2}$, $\mathbf{k_3}$ (in chronological order). The third-order polarization is then created along eight possible directions:

$$P^{(3)}(\mathbf{r}, \tau_4; t_3, t_2, t_1)) = \sum_{s=1}^{4} P^{(3)}(\mathbf{k}_s, \omega_s; t_3, t_2, t_1)\,\mathrm{e}^{\mathrm{i}\mathbf{k}_s\mathbf{r} - \mathrm{i}\omega_s\tau_4} + \mathrm{c.c}, \tag{41}$$

where $\mathbf{k}_s = \pm\mathbf{k_1} \pm \mathbf{k_2} \pm \mathbf{k_3}$ is the signal direction; $\omega_s = \pm\omega_1 \pm \omega_2 \pm \omega_3$ its frequency; $\mathbf{r}$ the average distance from the system to the detector; τ_4 the detection time; and t_3, t_2, t_1 are the time intervals separating the interactions with optical fields. The nonlinear polarization is related to the response function $S_s^{(3)}$ via

$$P^{(3)}(\mathbf{k}_s, \omega_s; t_3, t_2, t_1) = P_s^{(3)}(t_3, t_2, t_1) = S_s^{(3)}(t_3, t_2, t_1)\, e^{i(\pm\omega_1 \pm\omega_2 \pm\omega_3)t_1}\, e^{i(\pm\omega_1 \pm\omega_2)t_2}\, e^{i(\pm\omega_3)t_3}. \quad (42)$$

We further recast the signal in the frequency domain

$$P_s(\Omega_3, \Omega_2, \Omega_1) = \int\int\int P_s(t_3, t_2, t_1)\, e^{i\Omega_3 t_3}\, e^{i\Omega_2 t_2}\, e^{i\Omega_1 t_1}\, dt_3\, dt_2\, dt_1. \quad (43)$$

The $\mathbf{k_1} + \mathbf{k_2} + \mathbf{k_3}$ signal vanishes due to the dipole selection rules in our model. We further have the symmetry $P_s^{(3)}(-\mathbf{k}_s, -\omega_s; t_3, t_2, t_1) = P_s^{(3)*}(\mathbf{k}_s, \omega_s; t_3, t_2, t_1)$. This leaves us with three independent techniques $\mathbf{k_I} = -\mathbf{k_1} + \mathbf{k_2} + \mathbf{k_3}$, $\mathbf{k_{II}} = \mathbf{k_1} - \mathbf{k_2} + \mathbf{k_3}$ and $\mathbf{k_{III}} = \mathbf{k_1} + \mathbf{k_2} - \mathbf{k_3}$.

After drawing the relevant diagrams, we can write the expressions for the corresponding responses directly following the diagram rules given in the appendix D.1. These rules suffice for all third-order diagrams considered in this paper. Higher order (e.g. fifth and above) signals can be derived similarly by writing the time-domain expressions from the relevant diagram and performing the time-convolutions analytically. Note that the dipole operators (and the states they create or annihilate) are labeled by the order in real-time in which they operate.

In appendix E, we apply these rules in order to derive the third-order signals shown in loop diagrams of figures 5 and 6. For the $\mathbf{k_I}$ technique (figure 5) the contribution from diagrams I_b and I_c diagrams vanishes (compensated by $I_{a_1^0}$, $I_{a_2^0}$) as from harmonic oscillator. The remaining diagram (I_a) reads

$$\begin{aligned} P_I^{(3)}(\Omega_3, t_2, \Omega_1) = -2 \sum_{4,3,2,1} & \mu_4 \mu_3^* \mu_2^* \mu_1 \mathcal{G}_1^\star(-\Omega_1 + \omega_1)\, \mathcal{G}_1^\star(t_2)\, \mathcal{G}_2(t_2) \\ & \times \mathcal{G}_{32}(\Omega_3 - \omega_1 + \omega_2 + \omega_3 + E_1 + i\gamma_1)\, \Gamma^{(2)}_{32,41}(\Omega_3 - \omega_1 + \omega_2 + \omega_3 + E_1 + i\gamma_1) \\ & \times \mathcal{G}_{14}(\Omega_3 - \omega_1 + \omega_2 + \omega_3 + E_1 + i\gamma_1). \end{aligned} \quad (44)$$

Similarly, the only diagram contributing to $\mathbf{k_{II}}$ is shown in figure 6 (upper panel) diagram II_a

$$\begin{aligned} P_{II}^{(3)}(\Omega_3, t_2, \Omega_1) = -2 \sum_{4,3,2,1} & \mu_4 \mu_3^\star \mu_2 \mu_1^\star \mathcal{G}_1(t_2)\, \mathcal{G}_2^\star(t_2)\, \mathcal{G}_1(\Omega_1 + \omega_1) \\ & \times \mathcal{G}_{31}(\Omega_3 + \omega_1 - \omega_2 + \omega_3 + E_2 + i\gamma_2)\, \Gamma^{(2)}_{31,42}(\Omega_3 + \omega_1 - \omega_2 + \omega_3 + E_2 + i\gamma_2) \\ & \times \mathcal{G}_{24}(\Omega_3 + \omega_1 - \omega_2 + \omega_3 + E_2 + i\gamma_2). \end{aligned} \quad (45)$$

Two diagrams contribute to the $\mathbf{k_{III}}$ technique (diagrams III_a, III_b in figure 6 (lower panel)) and the resulting polarization is given by

$$\begin{aligned} P_{III}^{(3)}(\Omega_3, \Omega_2, t_1) = -2\theta(t_1) \sum_{1,2,3,4} & \mu_4 \mu_3 \mu_2^\star \mu_1^\star \mathcal{G}_1(t_1) \mathcal{G}_3(\Omega_3 + \omega_1 + \omega_2 - \omega_3)\, \mathcal{G}_4^\star(\Omega_2 - \Omega_3 + \omega_3) \\ & \times [\Gamma^{(2)}_{43,21}(\Omega_2 + \omega_1 + \omega_2)\, \mathcal{G}_{21}(\Omega_2 + \omega_1 + \omega_2) - \Gamma^{(2)}_{43,21}(\Omega_3 + \omega_1 + \omega_2 - \omega_3 + E_4 + i\gamma_4) \\ & \times \mathcal{G}_{21}(\Omega_3 + \omega_1 + \omega_2 - \omega_3 + E_4 + i\gamma_4)]. \end{aligned} \quad (46)$$

Equations (44)–(46) are fully specified by the structure of $\mathbf{\Gamma}^{(2)}$ in equations (33) and (28). They give succinct expressions for the various coherent signals obtained from a time-domain

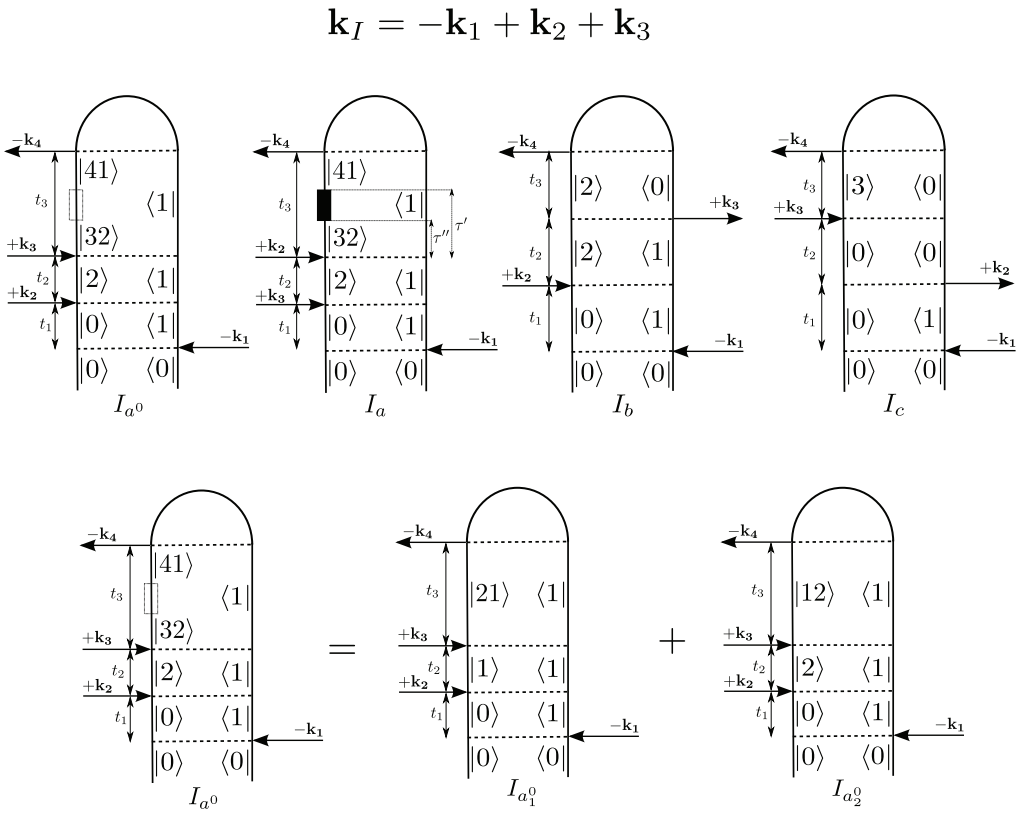

Figure 5. Loop diagrams for the third-order $\mathbf{k}_I = -\mathbf{k}_1 + \mathbf{k}_2 + \mathbf{k}_3$ technique. The black rectangle symbolizes the action of the scattering matrix while the dotted rectangle symbolizes the harmonic evolution in the two-exciton manifold (corresponding to the G^0 contribution in the Bethe–Salpeter equation). Diagram I_{a^0} can be split into two diagrams according to (B.2). The contribution from I_{a^0} cancels with that of diagrams I_b and I_c resulting in equation (44).

experiment of temporally well-separated pulses. Similar equations were obtained for the Frenkel exciton model in [19]. For completeness, these quasiparticle expressions are compared to the SOS expressions given in appendix F. The effects of coupling to a bath can be incorporated in the above signals by properly averaging the relevant products of Green's functions for each time interval. This is described in appendix G (figure 7).

5. Probing the three-exciton manifold by fifth-order signals

The general expressions for signals resulting from a series of temporally ordered pulses become cumbersome as one proceeds to higher-order optical processes with multiple time intervals. Nevertheless, the coboson expressions can readily be derived. This will be demonstrated below for four distinct five-pulse techniques.

We start with the $\mathbf{k}_s = 3\mathbf{k_1} - 2\mathbf{k_2}$ signal that results from three simultaneous interactions $3\mathbf{k_1}$ followed by evolution in the three-exciton manifold, then two simultaneous interactions $2\mathbf{k_2}$ followed by further evolution and then finally signal detection. This technique provides a clean look at the three-exciton manifold. In the rotating wave approximation, it is given by the three

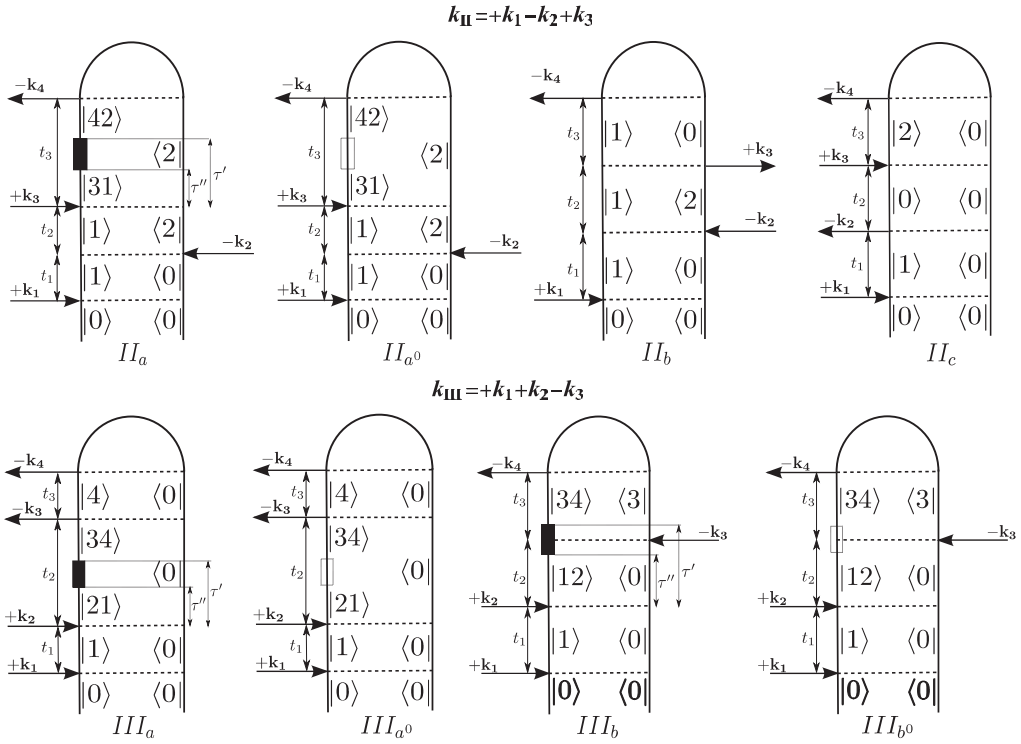

Figure 6. Top: loop diagrams for the $\mathbf{k}_{\mathrm{II}} = +\mathbf{k}_1 - \mathbf{k}_2 + \mathbf{k}_3$ technique. Since the free boson contributions must vanish, diagram II_{a^0} cancels with diagrams II_b and II_c resulting in equation (45). Bottom: loop diagrams for the $\mathbf{k}_{\mathrm{III}} = +\mathbf{k}_1 + \mathbf{k}_2 - \mathbf{k}_3$ technique. The free-boson diagrams, III_{a^0} and III_{b^0}, cancel each other.

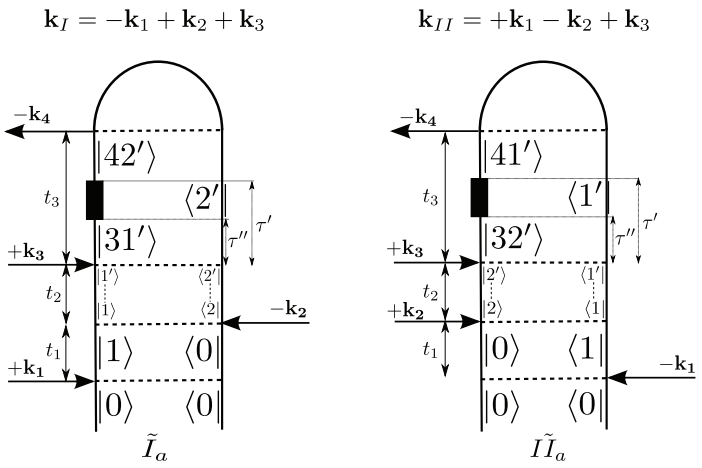

Figure 7. Left: loop diagram for the technique $\mathbf{k}_{\mathrm{I}} = -\mathbf{k}_1 + \mathbf{k}_2 + \mathbf{k}_3$ with transport included during the time period for which the density matrix is in a population (t_2). This diagram corresponds to equation (G.1). Right: loop diagram for the technique $\mathbf{k}_{\mathrm{II}} = +\mathbf{k}_1 - \mathbf{k}_2 + \mathbf{k}_3$ with transport similarly included. This diagram corresponds to equation (G.2).

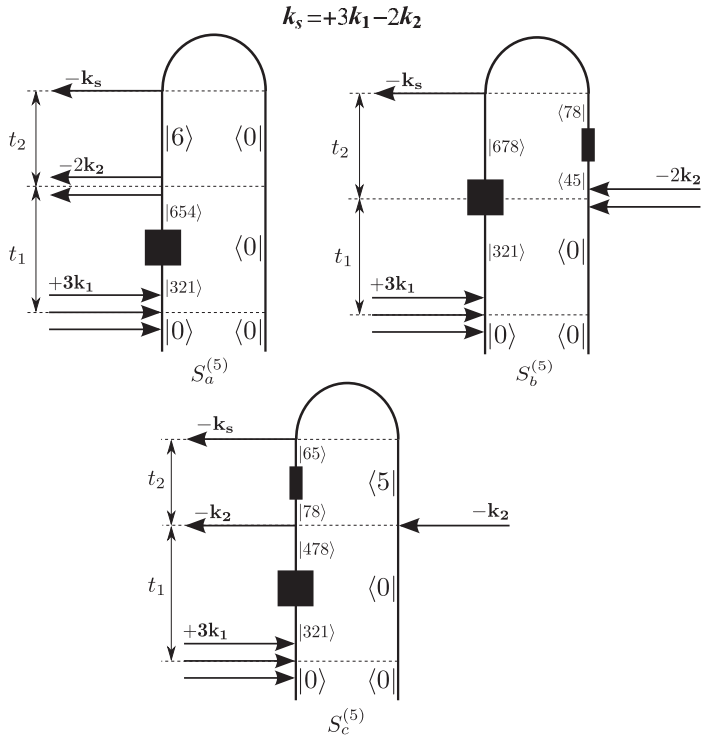

Figure 8. Loop diagrams for the fifth-order technique $\mathbf{k}_s = +3\mathbf{k}_1 - 2\mathbf{k}_2$ designed to probe three-exciton states. Black rectangles represent the action of the two-exciton scattering matrix and black squares represent the action of the three-exciton scattering matrix. States are labeled by the dipoles that create or annihilate them except where further dummy states are required (namely, between two scattering matrices). The signals corresponding to these diagrams are given in equations (48)–(50).

diagrams of figure 8(a)–(c):

$$S^{(5)}_{3\mathbf{k_1}-2\mathbf{k_2}} = S^{(5)}_{\mathrm{a}} + S^{(5)}_{\mathrm{b}} + S^{(5)}_{\mathrm{c}}. \tag{47}$$

We may then easily read the response off the three diagrams in terms of correlation functions following our rules. This gives

$$P^{(5)}_{\mathrm{a}}(\Omega_2, \Omega_1) = 6 \sum_{6,\ldots,1} \mu_6\mu_5\mu_4\mu_3^\star\mu_2^\star\mu_1^\star \mathcal{G}_6(\Omega_2 + 3\omega_1 - 2\omega_2)\, \mathcal{G}_{654}(\Omega_1 + 3\omega_3)\, \Gamma^{(3)}_{321,654} \times (\Omega_1 + 3\omega_3)\, \mathcal{G}_{321}(\Omega_1 + 3\omega_3)\,, \tag{48}$$

$$P^{(5)}_{\mathrm{b}}(\Omega_2, \Omega_1) = 12 \sum_{8,\ldots,1} \mu_6\mu_5\mu_4\mu_3^\star\mu_2^\star\mu_1^\star \mathcal{G}^\star_{45}(\Omega_2 - \Omega_1 - 2\omega_2)\, \Gamma^{(2),\star}_{45,78}(\Omega_1 - \Omega_2 + 2\omega_2) \times \mathcal{G}^\star_{78}(\Omega_2 - \Omega_1 - 2\omega_2)\, \mathcal{G}_{678}(\Omega_1 + 3\omega_3)\, \Gamma^{(3)}_{321,678}(\Omega_1 + 3\omega_1)\, \mathcal{G}_{321}(\Omega_1 + 3\omega_3)\,, \tag{49}$$

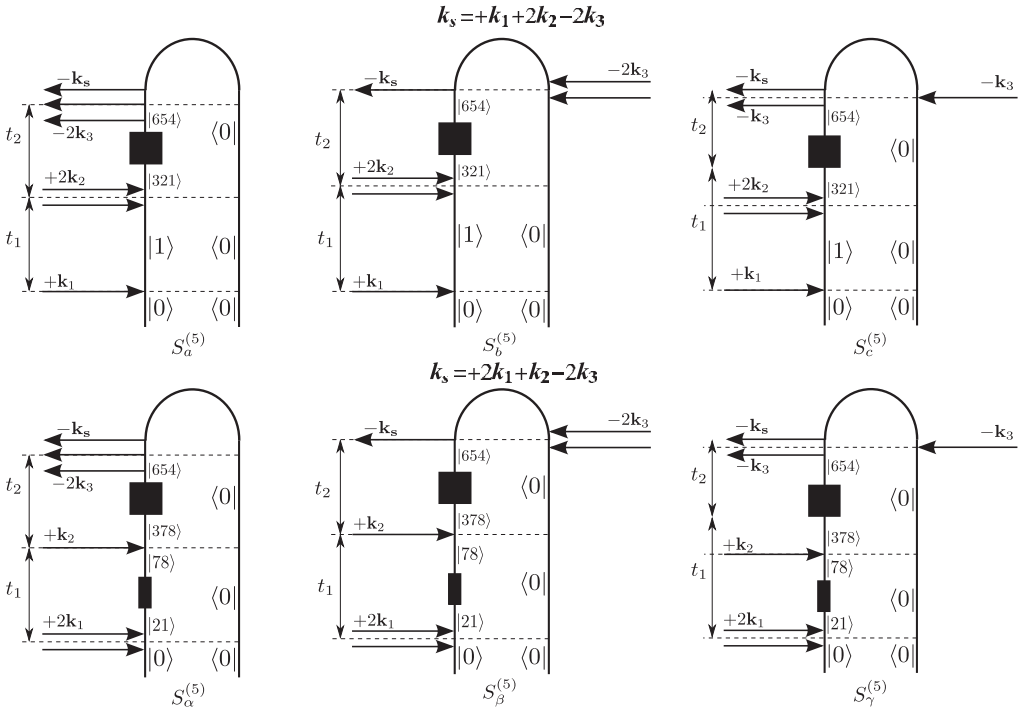

Figure 9. Top: loop diagrams for the fifth-order technique $\mathbf{k}_s = +\mathbf{k}_1 + 2\mathbf{k}_2 - 2\mathbf{k}_3$ which correlates the single- and triple-exciton manifolds. These three diagrams differ only by their sign which is determined by the number of interactions from the right. Thus, diagram (b) may be interpreted to cancel diagram (c) leaving equation (52). Bottom: loop diagrams for the technique $\mathbf{k}_s = +2\mathbf{k}_1 + \mathbf{k}_2 - 2\mathbf{k}_3$ which correlates the double- and triple-exciton manifolds. Note that these three diagrams also differ only by their sign which is determined by the number of interactions from the right. Thus, diagram $S_\beta^{(5)}$ may be interpreted to cancel diagram $S_\gamma^{(5)}$ leaving equation (54).

$$P_c^{(5)}(\Omega_2, \Omega_1) = 6 \sum_{8,\ldots,1} \mu_6\mu_5\mu_4\mu_3^\star\mu_2^\star\mu_1^\star \mathcal{G}_{65}(\Omega_2 + 3\omega_1 - 2\omega_2 + E_5 + i\gamma_5)$$
$$\times \Gamma^{(2)}_{78,65}(\Omega_2 + 3\omega_1 - 2\omega_2 + E_5 + i\gamma_5)$$
$$\times \mathcal{G}_{78}(\Omega_2 + 3\omega_1 - 2\omega_2 + E_5 + i\gamma_5)\mathcal{G}_{478}(\Omega_1 + 3\omega_1)\Gamma^{(3)}_{321,478}(\Omega_1 + 3\omega_1)$$
$$\times \mathcal{G}_{321}(\Omega_1 + 3\omega_1). \tag{50}$$

Note that diagram $S_b^{(5)}$ is split into two in the same way as diagram III_b of figure 6 (lower panel); however, this time both expressions are identical.

We next turn to the technique $\mathbf{k}_s = +\mathbf{k}_1 + 2\mathbf{k}_2 - 2\mathbf{k}_3$ in which the signal pulse $\mathbf{k}_s$ coincides temporally with $-2\mathbf{k}_3$. This is given by three diagrams shown in figure 9 (top). The diagrams differ only in their overall sign which is determined by $(-1)^N$ where N is the number of interactions from the right. Hence, the contribution from diagram β cancels that from γ (or α).

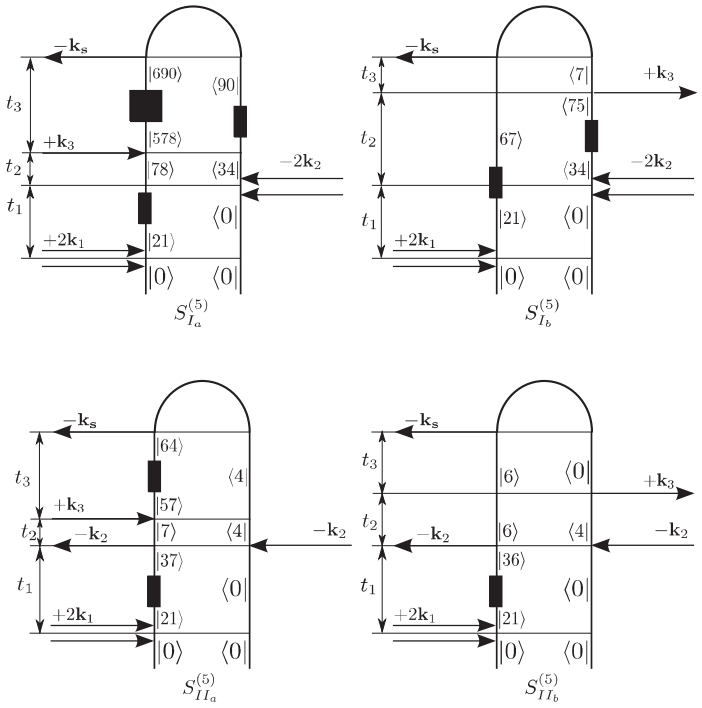

Figure 10. Loop diagrams for the $\mathbf{k}_s = +2\mathbf{k}_1 - 2\mathbf{k}_2 + \mathbf{k}_3$ technique. The signals from these diagrams are given in equations (55)–(58).

We may thus write the response in the time and frequency domains as

$$S^{(5)}_{a}(t_1, t_2) = 6 \sum_{6\ldots1} \mu_6\mu_5\mu_4\mu^{\star}_3\mu^{\star}_2\mu^{\star}_1 \int_0^{t_2} d\tau' \int_0^{\tau'} d\tau'' \mathcal{G}_{654}(t_2 - \tau')\Gamma^{(3)}_{321,654}(\tau' - \tau'')\mathcal{G}_{321}(\tau'')\mathcal{G}_1(t_1), \tag{51}$$

$$P^{(5)}_{a}(\Omega_1, \Omega_2) = 6 \sum_{6\ldots1} \mu_6\mu_5\mu_4\mu^{*}_3\mu^{\star}_2\mu^{\star}_1 \mathcal{G}_{654}(\Omega_2 + \omega_1 + 2\omega_2)\,\Gamma^{(3)}_{321,654}(\Omega_2 + \omega_1 + 2\omega_2)$$
$$\times \mathcal{G}_{321}(\Omega_2 + \omega_1 + 2\omega_2)\,\mathcal{G}_1(\Omega_1 + \omega_1)\,. \tag{52}$$

This technique probes correlations between the single (Ω_1) and triple (Ω_2) exciton manifolds.

We now turn to a third technique, $\mathbf{k}_s = +2\mathbf{k}_1 + \mathbf{k}_2 - 2\mathbf{k}_3$ (figure 9, bottom). The diagrams also differ only in their overall sign in exactly the same way as the diagrams from the previous technique. Thus, once again there is a cancellation of the contributions from diagrams β and γ (or α). The time and frequency-domain responses are

$$S^{(5)}_{\alpha}(t_1, t_2) = 6 \sum_{8\ldots1} \mu_6\mu_5\mu_4\mu^{*}_3\mu^{\star}_2\mu^{\star}_1 \int_0^{t_2} d\tau'_2 \int_0^{\tau'_2} \mathcal{G}_{654}\left(t_2 - \tau'_2\right)\Gamma^{(3)}_{321,654}\left(\tau'_2 - \tau''_2\right)\mathcal{G}_{321}\left(\tau''_2\right)$$
$$\times \int_0^{t_1} d\tau'_1 \int_0^{\tau'_1} d\tau''_1 \mathcal{G}_{78}\left(t_1 - \tau'_1\right)\Gamma^{(2)}_{21,78}\left(\tau'_1 - \tau''_1\right)\mathcal{G}_{21}\left(\tau''_1\right), \tag{53}$$

$$P^{(5)}_{\alpha}(\Omega_1, \Omega_2) = 6 \sum_{8\ldots1} \mu_6\mu_5\mu_4\mu^{\star}_3\mu^{\star}_2\mu^{\star}_1 \mathcal{G}_{654}(\Omega_2 + 2\omega_1 + \omega_2)\,\Gamma^{(3)}_{654,321}(\Omega_2 + 2\omega_1 + \omega_2)$$
$$\times \mathcal{G}_{321}(\Omega_2 + 2\omega_1 + \omega_2)\,\mathcal{G}_{78}(\Omega_1 + 2\omega_1)\,\Gamma^{(2)}_{78,21}(\Omega_1 - 2\omega_1)\,\mathcal{G}_{21}(\Omega_1 + 2\omega_1)\,. \tag{54}$$

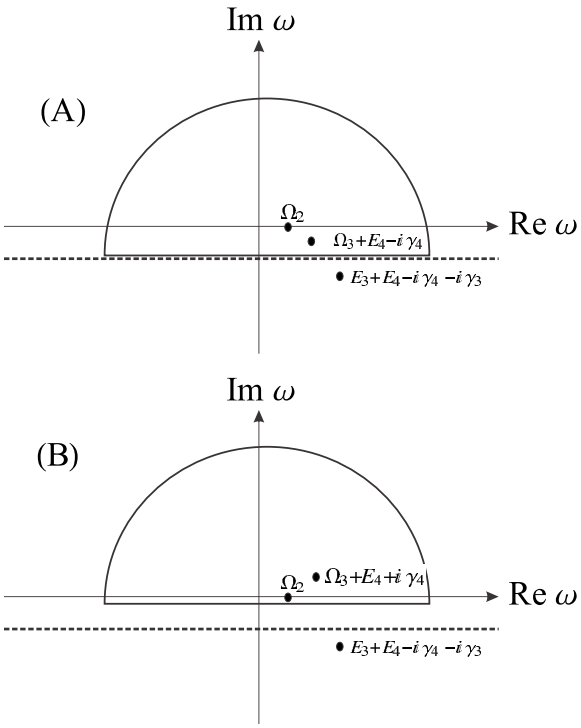

Figure 11. Two integration contours used in derivation of $\mathbf{k}_1+\mathbf{k}_2-\mathbf{k}_3$ (A) and $-\mathbf{k}_1+\mathbf{k}_2+\mathbf{k}_3$ (B) signals. The area under the dashed line contains two-exciton resonances.

This experiment probes correlations between the double (in Ω_1) and triple (in Ω_2) exciton manifolds.

Finally, we consider the fifth-order signal generated at $\mathbf{k}_s=+2\mathbf{k}_1-2\mathbf{k}_2+\mathbf{k}_3$. This technique is more complicated but can also look at two-exciton populations $|f\rangle\langle f|$. The signal is given by the four diagrams shown in figure 10

$$\begin{aligned}P^{(5)}_{\mathrm{I_a}}(\Omega_1,\Omega_2,\Omega_3)=-6\sum_{1,\ldots,7}\mu_6\mu_5^{\star}\mu_4\mu_3\mu_2^{\star}\mu_1^{\star}[&\mathcal{G}_{21}(\Omega_3+2\omega_1-2\omega_2+\omega_3+E_3+\mathrm{i}\gamma_3)\\&\times\Gamma^{(2)}_{21,67}(\Omega_3+2\omega_1-2\omega_2+\omega_3+E_3+\mathrm{i}\gamma_3)\,\mathcal{G}_{67}(\Omega_3+2\omega_1-2\omega_2+\omega_3+E_3+\mathrm{i}\gamma_3)\\&\times\mathcal{G}^{\star}_{75}(\Omega_3-\Omega_2+\omega_3+E_3+\mathrm{i}\gamma_3)\,\Gamma^{(2),\star}_{75,34}(\Omega_3-\Omega_2+\omega_3+E_3+\mathrm{i}\gamma_3)\\&\times\mathcal{G}^{\star}_{34}(\Omega_3-\Omega_2+\omega_3+E_3+\mathrm{i}\gamma_3)+\mathcal{G}_{21}(\Omega_1+2\omega_1)\,\Gamma^{(2)}_{21,67}(\Omega_1+2\omega_1)\,\mathcal{G}_{67}(\Omega_1)\\&\times\mathcal{G}^{\star}_{75}(\Omega_1-\Omega_2+2\omega_2)\,\Gamma^{(2),\star}_{75,34}(\Omega_1-\Omega_2+2\omega_2)\,\mathcal{G}^{\star}_{34}(\Omega_1-\Omega_2+2\omega_2)],\end{aligned}\tag{55}$$

$$\begin{aligned}P^{(5)}_{\mathrm{I_b}}(\Omega_1,\Omega_2,\Omega_3)=6\sum_{0,\ldots,9}\mu_6\mu_5^{\star}\mu_4\mu_3\mu_2^{\star}\mu_1^{\star}&\mathcal{G}_{21}(\Omega_1+2\omega_1)\,\Gamma^{(2)}_{21,78}(\Omega_1+2\omega_1)\,\mathcal{G}_{78}(\Omega_1+2\omega_1)\\&\times\mathcal{G}_{578}(\Omega_3+\Omega_1-\Omega_2+2\omega_1+\omega_3)\,\Gamma^{(3)}_{578,690}(\Omega_3+\Omega_1-\Omega_2+2\omega_1+\omega_3)\\&\times\mathcal{G}_{690}(\Omega_3+\Omega_1-\Omega_2+2\omega_1+\omega_3)\\&\times\mathcal{G}^{\star}_{90}(\Omega_1-\Omega_2+2\omega_2)\,\Gamma^{(2),\star}_{90,34}(\Omega_1-\Omega_2+2\omega_2)\,\mathcal{G}^{\star}_{34}(\Omega_1-\Omega_2+2\omega_2),\end{aligned}\tag{56}$$

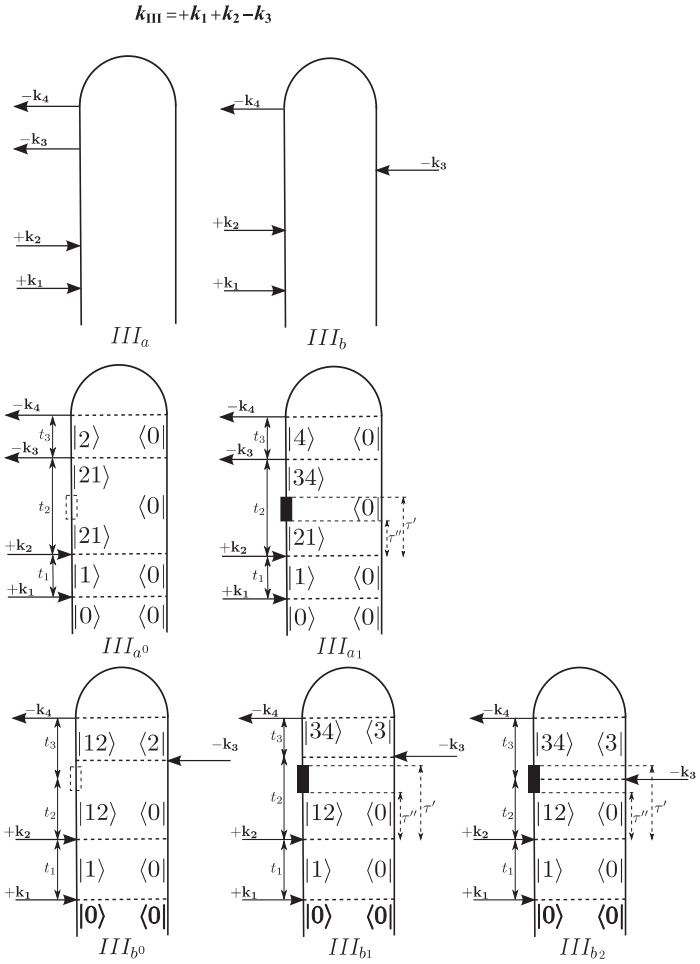

Figure 12. Loop diagrams for the $\mathbf{k}_{III}$ technique. The upper panel correspond to the signal written in terms of the dipole moment correlation functions. The first loop diagram in the Green's function representation (III_a) splits into two parts (III_{a0}, III_{a1}). III_{a0} describes the non-interacting part of the Dyson equation while III_{a1} contains the scattering matrix part. The second loop diagram III_b in the Green's function representation splits into three parts (III_{b0}, III_{b1} and III_{b2}). III_{b0} contains the non-interacting part of the two-exciton Green's function. III_{b1} is the part of the Dyson equation with the scattering matrix, when $\tau' < t_3$, while III_{b1} corresponds to the case when $\tau' > t_3$.

$$P^{(5)}_{\mathrm{II_a}}(\Omega_1,\Omega_2,\Omega_3) = 6\sum_{1,\ldots,6}\mu_6\mu_5^{\star}\mu_4\mu_3\mu_2^{\star}\mu_1^{\star}\mathcal{G}_{21}(\Omega_1+2\omega_1)\,\Gamma^{(2)}_{21,36}(\Omega_1+2\omega_1)$$
$$\times\mathcal{G}_{36}(\Omega_1+2\omega_1)\,\mathcal{G}_6(\Omega_2+2\omega_1-2\omega_2+E_4+\mathrm{i}\gamma_4)\,\mathcal{G}_6(\Omega_3+2\omega_1-2\omega_2+\omega_3)\,, \quad (57)$$

$$P^{(5)}_{\mathrm{II_b}}(\Omega_1,\Omega_2,\Omega_3) = -6\sum_{1,\ldots,7}\mu_6\mu_5^{\star}\mu_4\mu_3\mu_2^{\star}\mu_1^{\star}\mathcal{G}_{21}(\Omega_1+2\omega_1)\,\Gamma^{(2)}_{21,37}(\Omega_1+2\omega_1)\,\mathcal{G}_{37}(\Omega_1+2\omega_1)$$
$$\times\mathcal{G}_7(\Omega_2+2\omega_1-2\omega_2+E_4+\mathrm{i}\gamma_4)\,\mathcal{G}_{57}(\Omega_3+2\omega_1-2\omega_2+\omega_3+E_4+\mathrm{i}\gamma_4)\,\Gamma^{(2)}_{57,64}$$
$$\times(\Omega_3+2\omega_1-2\omega_2+\omega_3+E_4+\mathrm{i}\gamma_4)\,\mathcal{G}_{64}(\Omega_3+2\omega_1-2\omega_2+\omega_3+E_4+\mathrm{i}\gamma_4)\,. \quad (58)$$

Table 1. Parameters of the tight-binding Hamiltonian.

Parameter	Value
A	$350.0\,\mathrm{cm}^{-1}$
r_{ij}	4.5 Å
η	9.0 Å
k_e	$7.3\times10^5/\eta$
γ_i	$400\,\mathrm{cm}^{-1}$

Exciton annihilation of $|f\rangle\langle f|$ can be added to these expressions during t_2. This would be an interesting future extension (figures 11 and 12).

6. Numerical examples and discussion

We now demonstrate how the quasi-particle coboson formalism works in practice by applying it to a model system. The implementation is based on an approximate, tight-binding electronic Hamiltonian suited to describe single- and double-excitations in molecular aggregates [28]. We assume a linear chain of n coupled two-level systems separated by distance r. Electron spin is neglected. Double quantum coherence (DQC) signals are our technique of choice since they can be calculated by the SOS expressions without invoking the coboson formalism. We shall compare our results with those obtained in uncorrelated electron–hole basis by NEGF or SOS methods. We start with the Hamiltonian of single-excitations and double-excitations in the site basis given by equation (1). Simulations are presented for $N = 2, 3, 4$ atomic sites. The single-exciton manifold is constructed as a linear combination of on-site excitations (Frenkel) and charge-transfer excitations. The two-exciton manifold is represented by a basis set of non-interacting bosons. Pauli-allowed physical states are only a subspace of the two-exciton manifold. For the molecular dimer ($N = 2$) we represent the manifolds graphically in figure 14. As indicated earlier, the coboson basis for the two-exciton manifold is over-complete and non-orthogonal; this poses some difficulties in the SOS formalism by making the doubly excited Hamiltonian blocks $H^{(2)}$ singular (see appendix F for details). More precisely, the block is ill-conditioned. For bright, on-site excitations we assume a transition moment $\mu = 1$ au and charge-transfer excitations are assumed to be dark ($\mu = 0$ au). In other words, the transition dipole moment is proportional to the overlap between electron and hole wave functions. The sizes of the tetradic matrices $\boldsymbol{\lambda}$ and $\boldsymbol{\xi}$ are 4^4, $9^4 = 6561$ and $81^4 = 4.3 \times 10^7$ for $n = 2,\ 3$ and 4, respectively. These are also the sizes of the extended doubly excited manifolds. The electron and hole hopping amplitudes in our model $t^{(1)}_{m1,n1}$ and $t^{(2)}_{m2,n2}$ are assumed to decay exponentially with the separation r between chromophores $t^1_{m1,n1} = t^2_{m2,n2} = A * \exp(-|r_m - r_n|/\rho) \quad \text{for} \quad m \neq n$. The diagonal contributions are given by $5.0 * k_e/\eta \quad \text{for} \quad m = n$. Loosely speaking, this is an extension of the tight-binding model. The Hamiltonian parameters are summarized in table 1. In all calculations of the two-dimensional (2D)-DQC, spectra are based on the results of section 4 and we assume a common dephasing rate of single excitons $\gamma_i = 400\,\mathrm{cm}^{-1}$. The Coulomb attraction as well as electron–electron and hole–hole repulsion are assumed to have the truncated Coulomb form $V^{(i)}_{k1,n1} = W^{(1,2)}_{n1,m2} = (k_e/\eta)/(|r_k - r_n|/\eta + 1)$ where η is a cutoff distance. The modification of the denominator accounts for possible residence of the interacting particles on the same site which is necessary for the extended basis and is automatically removed

by the Pauli blocking of those states. The tetradic matrices $V^{(1)}_{l1k1,n1m1}$, $V^{(2)}_{l1k1,n1m1}$, $W^{(1,2)}_{l1k1,n1m1}$ describe electron–electron and hole–hole repulsion and electron–hole attraction, respectively. Assuming that the atomic orbitals are strongly localized [29], we define these tetradic matrices as $V^{(i)}_{l1k1,n1m1} = \delta_{l1,k1}\delta_{n1,m1}V^{(i)}_{k1,n1}$, $W^{(1,2)}_{n2n1,m2m1} = \delta_{n2,n1}\delta_{m2,m1}W^{(1,2)}_{n1,m2}$. The parameters of the electron–hole Hamiltonian (equation (1)) defined above allow us to calculate the elements of the electron–hole pair Hamiltonian (equation (6)). The choice of parameters results in a single electron–hole pair block of the Hamiltonian (equation (7)) with dominant diagonal coupling ($\mathbf{t}$) and weak off-diagonal $\mathbf{W}$ contributions. On the other hand, the two exciton block given by equation (8) is sparse. The single electron–hole pair block can be diagonalized numerically (equation (11)) yielding the eigenfunctions $\langle 1|m\rangle$. The Pauli exchange matrix can be projected on those states as in equation (19) yielding $\boldsymbol{\lambda}$. The Coulomb part of the two exciton block projected on those states via equation (16) gives the Coulomb direct scattering $\boldsymbol{\xi}$. Together, these tetradic matrices constitute the coboson algebra.

Before discussing any measurable signals, we shall briefly survey the structure and properties of the main ingredients required for their simulations: the Green's function and the scattering matrix. Specifically we shall discuss the deviation of the cobosons from ideal bosons on the level of the spectral function defined via the imaginary part of $\mathtt{Tr}(\mathbf{G}^{(2,0)}(\omega))$ for bosons and $\mathtt{Tr}(\mathbf{G}^{(2)}(\omega))$ for cobosons. The repeated actions of Pauli blocking and Coulomb scattering is demonstrated for a model dimer of coupled two-level systems in figure 13. The top panel depicts the two-boson spectral function. Here, resonances appear at the sum of the energy of the harmonic oscillators (arising from $\mathbf{U}^{(1)}$). Those are a useful measure of the number of possible permutations leading to a given bi-exciton like formation composed of two harmonic oscillators. Due to the bosonic properties, all possible permutations of double-excitations contribute. The lowest energy peak corresponds to bi-excitons composed of two subsequent charge-transfer excitations (figure 14). The high-energy peak correspond to two bright, on-site excitations. In between, we see all combinations of two subsequent excitations leading to a double excitation with two particles residing on the same site. The action of the Pauli-exclusion matrix $\boldsymbol{\Lambda}^{(2)}$ is only demonstrated in the middle panel of figure 13. It removes all double excitations with two particles residing on the same site leaving only two resonances (two-exciton states) in the spectral function. Coulomb interaction between cobosons is taken into account in the bottom panel of figure 13. Due to the anharmonic contributions contained in $\boldsymbol{\Gamma}^{(2)}$ (via $\boldsymbol{\Xi}^{(2)}$ as the projection of $\mathbf{U}^{(2)}$), the bright, two-exciton resonance degeneracy is lifted.

We can now turn to the DQC spectra depicted in figure 15. The signal vanishes for pure bosons. Thus, it provides a good measure of the anharmonicities which enter via two- and single-exciton coherences as cross-peaks. Formal analysis of the spectra is done by using the SOS expression given in appendix F. For a dimer, the effect of Pauli scattering is only shown in the top row of figure 15, as real (left) and imaginary (right) values. A single, two-exciton cross-resonance along the Ω_2-axis appears exactly at twice the energy of the bright single-exciton state (given along the Ω_3-axis). Coulomb scattering effects, as contained in $\boldsymbol{\Xi}^{(2)}$, are demonstrated in the second row of figure 15. The energy of the two-exciton resonance along Ω_2 is reduced as compared to that of double single-exciton transitions showing formation of a weakly bound bi-exciton. The cross-peak is split into two along Ω_3 showing the splitting of the fundamental $g \rightarrow e$ ground-state to single-exciton transition from the $e \rightarrow f$ single- to bi-exciton transition. The second possible two-exciton resonance (the low energy pole in the coboson spectral function) is dark in the DQC signal. The signals for $N = 3$ and 4 are depicted in the third and fourth row of figure 15 respectively. Due to increased exciton de-localization in

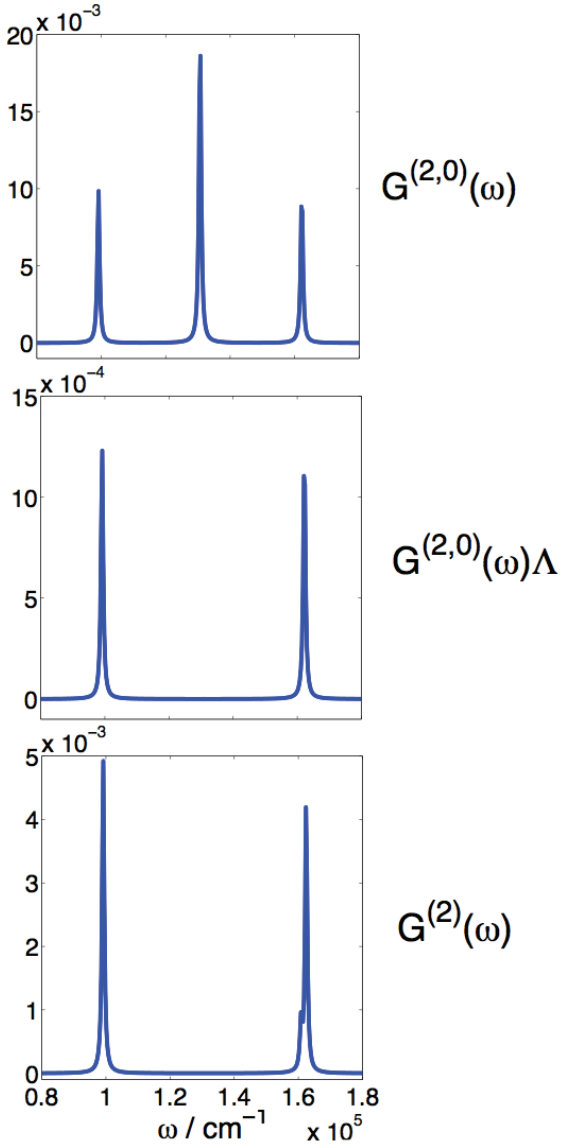

Figure 13. Top: the spectral function of non-interacting, two-exciton states given by the imaginary part of the trace of the non-interacting Green's function $G^{(2,0)}(\omega)$ (equation (B.2)). Middle: spectral function of two cobosons driven by the Pauli exchange only. Bottom: spectral function of two cobosons driven both by the Coulomb interaction and Pauli exchange (equation (22)) (bottom).

the linear chain of chromophores, the lowest energy bi-exciton state is further stabilized along Ω_2. In all depicted 2D-DQC spectra ($N = 2 - 4$), the fundamental $g \rightarrow e$ transition appears at the same Ω_3 frequency. The stabilization of the bi-exciton state by Coulomb scattering with increasing de-localization length causes the shift of the $e \rightarrow f$ single- to bi-exciton transition. For $n = 3$ an additional bi-exciton state (with weaker signal intensity) can be identified at higher Ω_2 values via its coherence with the same bright single exciton. One additional bi-exciton state

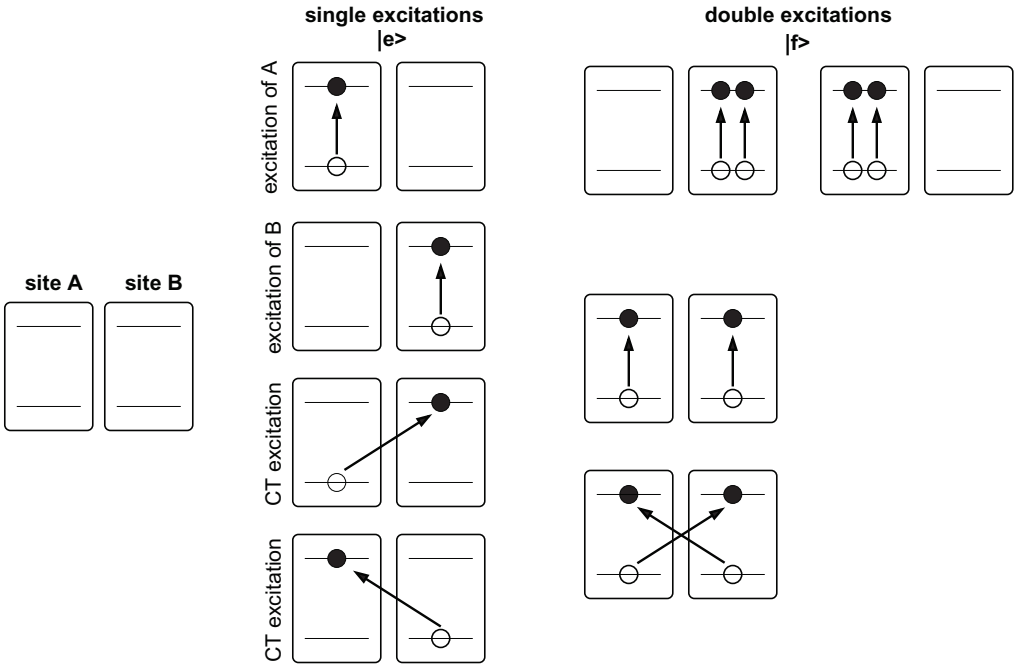

Figure 14. Single $|e\rangle$ and double $|f\rangle$ excitations of the molecular doublet (uncorrelated, electron–hole basis). The un-physical doubly excited states that must be included in the coboson description are shown in the right upper panel.

can be identified for $N = 4$. Now the $g \rightarrow e$ fundamental appears red-detuned from the $e \rightarrow f$ single- to bi-exciton transition.

7. Concluding remarks

We have developed a quasi-particle coboson, diagrammatic technique for computing high-order, nonlinear response functions. The approach is based on the Bethe–Salpeter and modified Dyson equations which define the coboson scattering matrices and relies solely on the coboson algebra. It does not suffer from the massive pathway cancellations that complicate the conventional SOS expressions. The algebra is completely defined by two-exciton interactions and may be readily derived from the original fermionic Hamiltonian. For any given number of excitons, this makes it possible to calculate high-order nonlinear response in terms of a sparse coboson scattering matrix $\mathbf{\Gamma}^{(n)}$. Applications are made to the third- and fifth-order responses which probe the two- and three-exciton manifolds, respectively. The single-exciton manifold, which can be extracted from standard calculations such as TDHF, TDFT [30–34], or the Bethe–Salpeter equation for fermions [35], fully defines the algebra. Many-body interactions are fully accounted for using products and combinations of two-body interactions: direct Coulomb scattering $\boldsymbol{\xi}$, and Pauli exchange $\boldsymbol{\lambda}$. Cobosons are more closely connected to optical measurements than the original fermion operators since each transition can be described by a single coboson rather than two fermions. In addition, taking into account the finite bandwidth of laser pulses, it should be possible to make drastic truncations of the relevant cobosons in a given measurement. This is not possible in the fermion representation and makes the calculations much more affordable even at the SOS level.

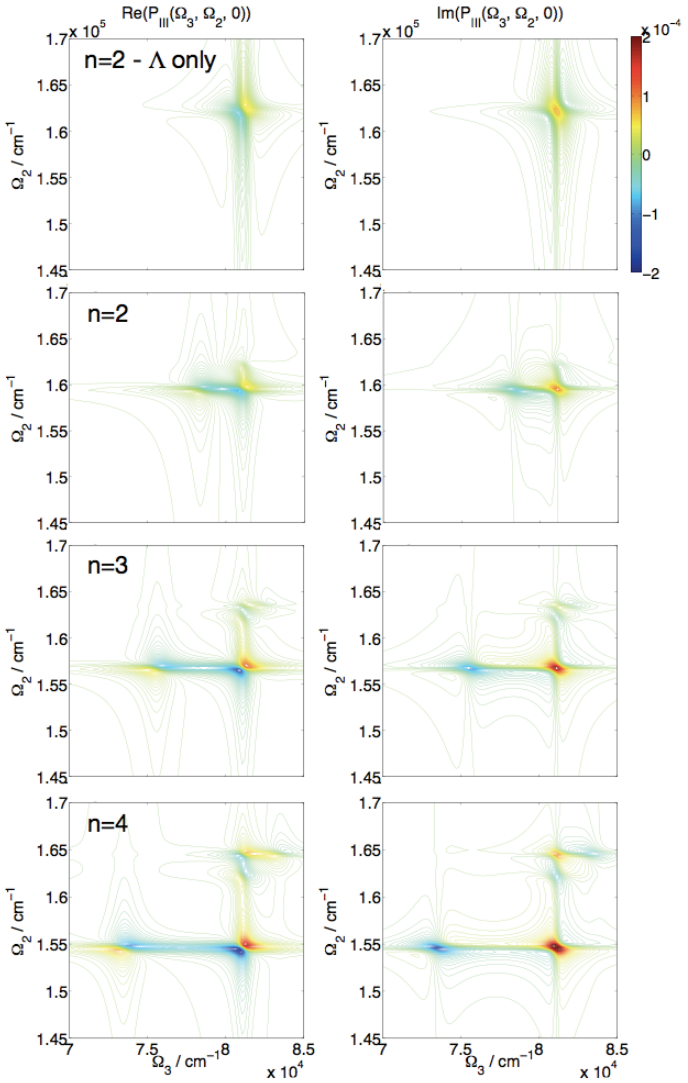

Figure 15. The 2D-DQC signal of a dimer ($N = 2$) including the action of the Λ matrix only (top), dimer with Coulomb scattering ($N = 2$, second row from top), trimer ($N = 3$, second row from bottom) and tetramer ($N = 4$, bottom)). Both the real (left) and imaginary parts (right) of the signal are shown.

Acknowledgments

We gratefully acknowledge the support of the National Science Foundation (NSF) through grant no. CHE-1058791 and from Chemical Sciences, Geosciences, and Biosciences Division, Office of Basic Energy Sciences, Office of Science, (US) Department of Energy (DOE). BPF gratefully acknowledges support from the Alexander-von-Humboldt Foundation through the Feodor–Lynen program.

Appendix A. Coboson algebra

- Pauli scattering:

$$[B_4,\, B_2^\dagger] = \delta_{4,2} - D_{4,2}, \tag{A.1}$$

$$[D_{4,2},\, B_1^\dagger] = \sum_3 \left(\lambda_{21,43} + \lambda_{21,34}\right) B_3^\dagger, \tag{A.2}$$

$$D_{4,2}|g\rangle = 0. \tag{A.3}$$

- Coulomb (direct) scattering:

$$[H,\, B_2^\dagger] = E_2 B_2^\dagger + V_2^\dagger, \tag{A.4}$$

$$[V_2^\dagger,\, B_1^\dagger] = \sum_{3,4} \xi_{21,43} B_4^\dagger B_3^\dagger, \tag{A.5}$$

$$V_2^\dagger|g\rangle = 0. \tag{A.6}$$

- Interaction expansion:

$$\frac{1}{\omega - H} B_2^\dagger = B_2^\dagger \frac{1}{\omega - H - E_2} + \frac{1}{\omega - H} V_2^\dagger \frac{1}{\omega - H - E_2}. \tag{A.7}$$

- Overcompleteness:

$$B_2^\dagger B_1^\dagger = -\sum_{4,3} \lambda_{21,43} B_4^\dagger B_3^\dagger, \tag{A.8}$$

$$I = \frac{1}{(N!)^2} \sum_{1,\ldots,N} B_1^\dagger \ldots B_N^\dagger |g\rangle\langle g| B_N \ldots B_1. \tag{A.9}$$

- $\mathcal{P}$ the electron–hole exchange tensor [18]:

$$\left[B_m,\, B_n^\dagger\right] = \delta_{mn} - 2 \sum_{kl} \mathcal{P}_{lk,nm} \hat{B}_k^\dagger \hat{B}_l, \tag{A.10}$$

$$\begin{aligned} \mathcal{P}_{lk,nm} &= \mathcal{P}^{(1)}_{lk,nm} + \mathcal{P}^{(2)}_{lk,nm}, \\ \mathcal{P}^{(1)}_{lk,nm} &= \tfrac{1}{2}\delta_{m1,l1}\delta_{n1,k1}\delta_{m2,n2}\delta_{k2,l2}, \\ \mathcal{P}^{(2)}_{lk,nm} &= \tfrac{1}{2}\delta_{m2,l2}\delta_{n2,k2}\delta_{m1,n1}\delta_{k1,l1}. \end{aligned} \tag{A.11}$$

Tetradic/hexadic matrix notation. In Combescot's work and elsewhere, matrix elements are sometimes specified by

$$A_{43,21} = A \begin{pmatrix} 4 & 1 \\ 3 & 2 \end{pmatrix}, \tag{A.12}$$

$$A_{654,321} = A \begin{pmatrix} 6 & 1 \\ 5 & 2 \\ 4 & 3 \end{pmatrix}. \tag{A.13}$$

Those are rank $2n$ tensors and can be mapped on the regular (rank 2) matrices by adopting the notation for an arbitrary matrix $A_{\mathtt{row,col}}$ where `row` and `col` are given as elements of $n \otimes \cdots \otimes 1$. Practically, we construct the tensors in Mathematica as the following table:

```
Tensor‘Indices =table[{e[1],e[2],...,e[2n]},
            {e[1],1,NumberOfExcitons},...,{e[2n],1,NumberOfExcitons}];
Tensor‘A=Map[A[[#1,#(n+1),...,#n,#2n]]&,Tensor‘Indices];
Matrix‘A=ArrayFlatten@Tensor‘A;
```

this yields the BlockMatrix whose elements are $2n$–2-rank tensors and so on till the regular matrices. Function `ArrayFlatten` provides the mapping to the regular matrix manifold. The back-mapping to the tensor is provided by

```
Tensor‘A = Partition[Matrix‘A,ConstantArray[NumberOfExcitons,2*n-2]].
```

The transpose of a tetradic matrix is $A^{\mathrm{T}}_{43,21} = A_{21,43}$ and the matrix product is $A_{43,21} = \sum_{4',3'} B_{43,4'3'} C_{4'3',21}$. For the sixtic matrices we have $A_{654,321} = \sum_{3'2'1'} B_{654,3'2'1'} C_{3'2'1,321}$.

Appendix B. The two-exciton Green's function and the scattering matrix

Here, we derive the Green's functions, the exciton scattering matrices and transition dipole moments in the coboson representation. For clarity, we present the main results first and then elaborate on the significance of the various terms and parameters. This section is essential for the subsequent calculations of all nonlinear signals. The key matrix equation to obtain the $n \geqslant 2$ coboson Green's functions $\mathbf{G}^{(n)}$ is the modified Dyson equation (26). Compared with the Bethe–Salpeter equation (22), this yields the exciton scattering matrix (equation (33)) whose components are the main subject of this appendix.

We start with the two-exciton manifold ($n = 2$). The matrix elements of the two-exciton Green's function are defined via

$$G^{(2)}_{12,34}(\omega) = \langle g | B_4 B_3 \frac{1}{\omega - H + \mathrm{i}\eta} B_2^\dagger B_1^\dagger | g \rangle. \tag{B.1}$$

The zero-order coboson Green's function $G^{(2,0)}$ is obtained by treating the excitons as structureless and non-interacting bosons

$$G^{(2,0)}_{12,34}(\omega) = \frac{\delta_{4,2}\delta_{3,1}}{\omega - E_1 - E_2 + \mathrm{i}\eta}. \tag{B.2}$$

The full form of the two-coboson Green's function requires the identity

$$\langle g | B_4 B_3 B_2^\dagger B_1^\dagger | g \rangle = \delta_{4,2}\delta_{3,1} + \delta_{3,2}\delta_{4,1} - \lambda_{21,43} - \lambda_{21,34} \tag{B.3}$$

which is obtained by (i) moving B_3 to the right to finally act on the ground state and (ii) using the Pauli scattering commutation relations (A.1). By means of the interaction expansion in appendix A, we can shift $\frac{1}{\omega - H + \mathrm{i}\eta}$ in the two-exciton Green's function (B.1) to the right so

that it finally acts on the ground state. After some straightforward but lengthy algebra utilizing equation (A.7), this procedure leads to

$$G^{(2)}_{12,34}(\omega) = \frac{1}{\omega - E_1 - E_2 + \mathrm{i}\eta}\langle g|B_4 B_3 B_2^\dagger B_1^\dagger|g\rangle + \frac{1}{\omega - E_1 - E_2 + \mathrm{i}\eta} \times \sum_{3',4'} \xi_{21,4'3'}\langle g|B_4 B_3 \frac{1}{\omega - H + \mathrm{i}\eta} B_{4'}^\dagger B_{3'}^\dagger|g\rangle. \tag{B.4}$$

By utilizing equation (B.3) the above expression (B.4) can be recast in the more compact matrix notation of modified Dyson equation (26) with parameters given by equation (27) From equation (19), we can see that $\boldsymbol{\lambda}$ is symmetric to simultaneous interchange of both pairs of indices (i.e. $\lambda_{21,43} = \lambda_{12,34}$). The Green's function (equation (B.4)) assumes a simpler form when $\boldsymbol{\xi}$ vanishes (as in small enough quantum dots) and all nonlinearities are caused by Pauli exclusion alone: $\mathbf{G}^{(2)} = \mathbf{G}^{(2,0)}(\boldsymbol{\Delta}^{(2)} - \boldsymbol{\Lambda}^{(2)})$. From the form of the $\boldsymbol{\Lambda}^{(2)}$ matrix, it is clear that the Green's functions vanish when the two excitons try to occupy the same state (i.e. $G^{(2)}_{11,11} = 0$). Therefore the Pauli exchange matrix is responsible for removing those unphysical states caused by over-completeness of the coboson basis.

Subtracting equation (22) from equation (26) and multiplying by $(\mathbf{G}^{(2,0)})^{-1}$ from the left, we obtain

$$\boldsymbol{\Gamma}^{(2)}\mathbf{G}^{(2,0)} = \boldsymbol{\Xi}^{(2)}\mathbf{G}^{(2)} - \boldsymbol{\Lambda}^{(2)}. \tag{B.5}$$

Note that this equation is different from its counterpart in the electron–hole representation (see equation (B4) of [18]). Putting equation (B.5) back into equation (22) now gives

$$\boldsymbol{\Xi}^{(2)}\mathbf{G}^{(2)} = (\mathbf{I} - \boldsymbol{\Xi}^{(2)}\mathbf{G}^{(2,0)})^{-1}\boldsymbol{\Xi}^{(2)}\mathbf{G}^{(2,0)}(\boldsymbol{\Delta}^{(2)} - \boldsymbol{\Lambda}^{(2)}). \tag{B.6}$$

By substituting this equation into equation (B.5), we finally obtain the two-exciton scattering matrix (equation (33)). This is the exact coboson counterpart of the electron–hole expression in [18, (equation (D1))].

Appendix C. The three-excitons Green's function

The three-exciton Green's function is defined by

$$G^{(3)}_{123,456}(\omega) = \langle g|B_6 B_5 B_4 \frac{1}{\omega - H + \mathrm{i}\eta} B_3^\dagger B_2^\dagger B_1^\dagger|g\rangle. \tag{C.1}$$

At this point we introduce several axillary quantities, expressed in the form of sixtic matrices. The first is the non-interacting exciton Green's function

$$G^{(3,0)}_{123,456}(\omega) = \frac{\delta_{1,4}\delta_{2,5}\delta_{3,6}}{\omega - E_3 - E_2 - E_1 + \mathrm{i}\eta}. \tag{C.2}$$

The second is the Pauli blocking indicator (PBI) matrix, similar to equation (B.3)

$$\tilde{\lambda}_{123,456} = \langle g|B_6 B_5 B_4 B_3^\dagger B_2^\dagger B_1^\dagger|g\rangle = \Delta^{(3)}_{123,456} - \tilde{\Lambda}^{(3)}_{123,456} \tag{C.3}$$

with the parameters given by equations (25) and (30). Equation (C.3) has been obtained by moving B_4 in equation (C.1) all the way to the right so that it finally acts on the ground state. Pauli scattering (equation (A.1)) is used and the corresponding Shiva diagrams are given in figure 2.

When the Coulomb coupling is neglected, the Green's function becomes

$$G^{(3)}_{123,456}(\omega) = \frac{1}{\omega - E_3 - E_2 - E_1 + \mathrm{i}\eta}\tilde{\lambda}_{123,456}. \tag{C.4}$$

The matrix elements of $\tilde{\boldsymbol{\lambda}}$ can be viewed as flags switching on and off the Green's function matrix elements in order to maintain Pauli blocking and conservation of energy. The first term in the PBI (equation (C.3)) assures energy conservation in the absence of external perturbations. That is, only diagonal elements are flagged on. There are 3! ways to exchange the excitons and still conserve energy. The second PBI term can switch off some of those flags in accordance to Pauli blocking modeled by single-exchange (two-coboson) elements $\boldsymbol{\lambda}$. This occurs when two cobosons try to share the same site. The latter case is described by the part of the $\boldsymbol{\lambda}$ matrix with $n1 = n2$ and $l1 = l2$ so that $\lambda_{12,34} = \delta_{1,3}\delta_{2,4}$. However in the case of three cobosons we have 12 (see $\tilde{\boldsymbol{\lambda}}^{(0)}$ of equation (30)) uncompensated negative terms. These terms are compensated by the third part of the PBI of equation (31). Contribution from $\tilde{\boldsymbol{\lambda}}^{(1)}$ restores those negative flags back to zero making the exchange via virtual excitons in the three coboson manifold. The net Green's function thus vanishes when the underlying electrons and holes have the same quantum numbers and sites.

In the general case (retaining the Coulomb interactions), after lengthy but straightforward application of the algorithm for shifting the Green's function operator $1/(\omega - \hat{H} + \mathrm{i}\eta)$ all the way to the right and using the interaction expansion, we obtain coupled system of Dyson equations for $\mathbf{G}^{(3)}$ and an auxiliary matrix $\tilde{\mathbf{G}}^{(3)}$:

$$\begin{aligned}\tilde{G}^{(3)}_{123,456}(\omega) &= \langle g|B_6B_5B_4B_3^{\dagger}\frac{1}{\omega - H - E_3 + \mathrm{i}\eta}B_2^{\dagger}B_1^{\dagger}|g\rangle \\ &= \frac{1}{\omega - E_3 - E_2 - E_1 + \mathrm{i}\eta}\left(\tilde{\lambda}_{123,456} + \sum_{3',2',1'}\tilde{\xi}^{(3,1)}_{123,1'2'3'}\tilde{G}^{(3)}_{1'2'3',456}(\omega)\right),\end{aligned} \tag{C.5}$$

$$\begin{aligned}G^{(3)}_{123,456}(\omega) ==& \frac{1}{\omega - E_3 - E_2 - E_1 + \mathrm{i}\eta} \\ &\left(\tilde{\lambda}_{123,456} + \sum_{3',2',1'} 2\xi^{(2,1)}_{123,1'2'3'}\tilde{G}^{(3)}_{1'2'3',456} + \left(\tilde{\xi}^{(3,1)}_{123,1'2'3'} + \tilde{\xi}^{(3,2)}_{123,1'2'3'} + \tilde{\xi}^{(3,3)}_{123,1'2'3'}\right), G^{(3)}_{1'2'3',456}\right)\end{aligned} \tag{C.6}$$

where $\tilde{\boldsymbol{\xi}}^{(3)}$ is given by equations (32).

We next use the hexadic matrices multiplication convention in appendix A in order to recast equations (C.6), (C.5) in a compact matrix form:

$$\tilde{\mathbf{G}}^{(3)} = \mathbf{G}^{(3,0)}(\boldsymbol{\Delta}^{(3)} - \tilde{\boldsymbol{\Lambda}}^{(3)}) + \mathbf{G}^{(3,0)}\tilde{\boldsymbol{\xi}}^{(3,1)}\tilde{\mathbf{G}}^{(3)}, \tag{C.7}$$

$$\mathbf{G}^{(3)} = \tilde{\mathbf{G}}^{(3)} + \mathbf{G}^{(3,0)}\tilde{\boldsymbol{\xi}}^{(3,1)}\tilde{\mathbf{G}}^{(3)} + \mathbf{G}^{(3,0)}\left(\boldsymbol{\Xi}^{(3)}\right)\mathbf{G}^{(3)} \tag{C.8}$$

with the parameters $\tilde{\boldsymbol{\Lambda}}^{(3)}$ and $\boldsymbol{\Xi}^{(3)}$ given by equations (28)–(30). The Shiva diagrams in figure 3 illustrate the single and two coboson interactions involved in the above system of equations.

The pure Pauli driven exchange between two ($\tilde{\boldsymbol{\lambda}}^{(0)}$) and three ($\tilde{\boldsymbol{\lambda}}^{(1)}$) cobosons (first term in equation (C.7)) as well as the direct Coulomb scattering between the two coboson $\boldsymbol{\Xi}^{(3)}$ (third term in equation (C.8)) are explicit. The second exchange-correlation term in equation (C.7) deserves special attention. If we expand the Dyson equation (C.7) into the infinite series, there will be direct-Coulomb terms $\tilde{\boldsymbol{\xi}}^{(3,1)}\mathbf{G}^{(3,0)}\tilde{\boldsymbol{\xi}}^{(3)}$, as well as mixed Pauli–Coulomb exchange terms $\tilde{\boldsymbol{\lambda}}^{(0,1)}\tilde{\boldsymbol{\xi}}^{(3,1)}\mathbf{G}^{(3,0)}\tilde{\boldsymbol{\xi}}^{(3,1)}$, $\tilde{\boldsymbol{\xi}}^{(3,1)}\tilde{\boldsymbol{\lambda}}^{(0,1)}\mathbf{G}^{(3,0)}\tilde{\boldsymbol{\xi}}^{(3,1)}$, etc. Corresponding Shiva diagrams are given in figure 6 of [36].

We can exclude $\tilde{\mathbf{G}}^{(3)}$ from equation (C.8) by recasting equation (C.7) in the form

$$\tilde{\mathbf{G}}^{(3)} = \left(\mathbf{I} - \mathbf{G}^{(3,0)}\boldsymbol{\xi}^{(3,1)}\right)^{-1}\mathbf{G}^{(3,0)}(\boldsymbol{\Delta}^{(3)} - \tilde{\boldsymbol{\Lambda}}^{(3)}).$$

This yields a single Dyson equation for the three-exciton Green's function in equation (26) with parameters given in equation (28).

Appendix D. Algorithm for computing the fifth-order techniques

1. Write the dipole operators, Green's functions and any relevant scattering matrices, in the order in which they appear on the loop as we move clockwise per the general instructions given in section D.1.
2. For all periods of evolution during which multi-exciton manifolds are not accessed, simply replace the time arguments of the Green's functions and any scattering matrices for that evolution with their Fourier-conjugate frequencies when they appear on the left side of the loop and with the negatives of their conjugate frequencies when on the right side. As an example, compare the t_1 and t_2 evolutions in diagram $\mathrm{I_a}$ of figure 4 with the corresponding Green's functions in equation (44).
3. Periods of evolution during which a scattering matrix is active on one branch of the loop and an interaction occurs on the other must be treated differently. In these cases, the Green's functions and scattering matrices (if any) corresponding to the state resulting from the interaction have their arguments shifted by the Fourier frequency that is conjugate to the time period during which the original scattering matrix was active but before the interrupting interaction. For a concrete example of how this works, observe the shifting of the arguments of the Green's functions and equation (49) that correspond to the bra side of the t_3 evolution and t_2 evolution in diagrams $\mathrm{III_b}$ and $S_{\mathrm{b}}^{(5)}$ respectively in figures 5 and 6. Finally, the arguments of the Green's function and scattering matrix corresponding to the 'interrupted' multi-excitonic evolution are simply the Fourier-conjugate frequency to the period of time before the interrupting interaction (compare the t_2 evolution and t_1 evolution in diagrams $\mathrm{III_b}$ and $S_{\mathrm{b}}^{(5)}$ respectively in figures 5 and 6 with equation (49)).
4. For all periods of multi-exciton evolution along the loop during which the density matrix is in a coherence with the single-exciton manifold (e.g. the coherence with the single-exciton state $\langle 1|$ in diagram $\mathrm{I_a}$ of figure 4), add the energy and dephasing of the relevant single-exciton state to the Fourier-conjugate frequency of the Green's functions and scattering matrix corresponding to the multi-exciton time period. This incorporates the evolution of the single-exciton state; therefore, we then omit the Green's function corresponding to its evolution. Note that this step applies also to those cases described in step 3 for which the interrupting interaction takes us to the first excitonic manifold as in diagram $\mathrm{III_b}$ of figure 5.

D.1. Loop diagram rules in the time domain

TD1. The loop represents the density operator. Its left branch stands for the ket, the right corresponds to the bra.

TD2. Each interaction with a field mode is represented by an arrow pointing to the left or right and acting on either the ket or the bra.

TD3. Arrows pointing to the right represent field annihilation operators and arrows pointing to the left represent field creation operators. This is made explicit by dressing the arrow with appropriate wave vectors $\pm\mathbf{k}_j$.

TD4. Within the rotating wave approximation, each interaction with a field annihilation operator is accompanied by the dipole operator $\mu^\dagger$, which leads to the excitation of the state represented by the ket and de-excitation of the state represented by the bra. Arrows pointing 'inwards' (i.e. pointing to the right on the ket and to the left on the bra) consequently cause absorption of a photon by exciting the system, whereas arrows pointing 'outwards' represent de-exciting the system by photon emission.

TD5. The interaction at the observation time is always the last. As a convention, it is chosen to occur from the left. This choice is arbitrary and does not affect the result.

TD6. The overall sign of the correlation function is given by $(-1)^{N_\mathrm{R}}$ where N_R is the number of interactions from the right.

TD7. Since the loop time goes clockwise along the loop, periods of evolution on the left branch correspond to retarded Green's functions while periods of evolution on the right branch correspond to advanced Green's functions.

D.2. Loop diagram rules in the frequency-domain

FD1. Time runs along the loop clockwise from bottom left to bottom right.

FD2. Each interaction with a field mode is represented by an arrow as in the time domain.

FD3. Arrows pointing to the right represent field annihilation operators and arrows pointing to the left represent field creation operators. This is made explicit by dressing the arrow with appropriate wave vectors $\pm\mathbf{k}_j$.

FD4. Within the rotating wave approximation, each interaction with a field annihilation operator is accompanied by the dipole operator $\mu^\dagger$, which leads to excitation of the material system. Arrows pointing to the right cause absorption of a photon by exciting the molecule, whereas arrows pointing to the left represent de-exciting the system by photon emission.

FD5. The interaction at the observation time is fixed to be with the detected mode and is always the last. It is chosen to occur on the left branch of the loop. This choice is arbitrary and does not affect the result.

FD6. Since the loop time goes clockwise along the loop, periods of evolution on the left branch correspond to retarded Green's functions while periods of evolution on the right branch correspond to advanced Green's functions.

FD7. The frequency arguments of the various Green's functions are cumulative. That is, they are given by the sum of all 'earlier' interactions along the loop.

FD8. A diagram carries a factor of $(-1)^{N_\mathrm{R}}$ where N_R is the number of interactions from the right.

Appendix E. Derivation of the third- and fifth-order time-domain response functions

Examining first the third-order response in the $\mathbf{k_I}$ technique, it is clear from the diagrams that the excited-state emission (ESE) and ground-state bleaching (GSB) processes (diagrams I_b and I_c respectively of figure 5) never have more than one exciton. Their evolution is thus harmonic. However, the excited-state absorption (ESA) process (I_a in figure 5) includes a period where two excitons are present. We will use the Bethe–Salpeter equation for the two-exciton Green's function. The first term in this equation represents free-boson evolution in the two-exciton manifold (represented by diagram I_{a^0} in figure 5) while the second term represents the anharmonicity. Since the nonlinear response from a harmonic oscillator vanishes, we know that the harmonic evolution of the ESA process must cancel with the sum of the ESE and GSB processes. We may thus express the nonlinear response in the $\mathbf{k_I}$ direction by a single term (diagram I_a of figure 5)

$$S_{\mathrm{I}}^{(3)}(t_3,t_2,t_1)$$
$$= -\theta(t_1)\,\theta(t_2)\,\theta(t_3)\int_0^{t_3}\mathrm{d}\tau'\int_0^{\tau'}\mathrm{d}\tau''\langle\hat{\mu}^-\hat{G}^{(1),\dagger}(t_1+t_2+t_3)\hat{\mu}^-\hat{G}^{(2,0)}(t_3-\tau')\Gamma^{(2)}(\tau'-\tau'')$$
$$\times\hat{G}^{(2,0)}(\tau'')\hat{\mu}^+\hat{G}^{(1)}(t_2)\hat{\mu}^+\rangle. \tag{E.1}$$

Similarly, in the $\mathbf{k_{II}}$ technique, a harmonic cancellation occurs and the signal is merely given by the anharmonic portion of the only diagram to include multiple excitons (diagram II_a in figure 6). Hence

$$S_{\mathrm{II}}^{(3)}(t_3,t_2,t_1)$$
$$= -\theta(t_1)\,\theta(t_2)\,\theta(t_3)\int_0^{t_3}\mathrm{d}\tau'\int_0^{\tau'}\mathrm{d}\tau''\langle\hat{\mu}^-\hat{G}^{(1),\dagger}(t_2+t_3)\hat{\mu}^-\hat{G}^{(2,0)}(t_3-\tau')\Gamma^{(2)}(\tau'-\tau'')$$
$$\times\hat{G}^{(2,0)}(\tau'')\hat{\mu}^+\hat{G}^{(1)}(t_1+t_2)\hat{\mu}^+\rangle. \tag{E.2}$$

For the $\mathbf{k_{III}}$ signal, both diagrams access the two-exciton manifold. Still, since the harmonic portion must cancel, the signal may be written as the sum of the anharmonic contributions from each diagram (III_a and III_b in figure 6):

$$S_{\mathrm{III}}^{(3)}(t_3,t_2,t_1) = -\theta(t_3)\theta(t_2)\theta(t_1)\left[\int_0^{t_2+t_3}\mathrm{d}\tau'\int_0^{\tau'}\mathrm{d}\tau''\langle\hat{\mu}^-\hat{G}^{(1),\dagger}(t_3)\hat{\mu}^-\hat{G}^{(2,0)}(t_2+t_3-\tau')\right.$$
$$\times\Gamma^{(2)}(\tau'-\tau'')\hat{G}^{(2,0)}(\tau'')\hat{\mu}^+\hat{G}^{(1)}(t_1)\hat{\mu}^+\rangle$$
$$-\int_0^{t_2}\mathrm{d}\tau'\int_0^{\tau'}\mathrm{d}\tau''\langle\hat{\mu}^-\hat{G}^{(1)}(t_3)\hat{\mu}^-\hat{G}^{(2,0)}(t_2-\tau')$$
$$\left.\times\,\Gamma^{(2)}(\tau'-\tau'')\hat{G}^{(2,0)}(\tau'')\hat{\mu}^+\hat{G}^{(1)}(t_1)\hat{\mu}^+\rangle\right]. \tag{E.3}$$

To evaluate these correlation functions, we simply insert the resolution of the identity matrix given in the appendix (equation (A.9)) between all Green's functions and dipole operators. First however, we will use the fact (shown in equation (F.9)) that, for the two-exciton dipole moments, $\boldsymbol{\mu} = \boldsymbol{\mu}^{(0)}(\mathbf{I}-\boldsymbol{\lambda})$, where, according to our convention, $\boldsymbol{\mu}^{(0)}$ is the dipole for a harmonic oscillator.

Using the over-completeness relation defined in the appendix and the definition of the Green's function defined in equation (B.1), it is easily verified that $\mathbf{G}^{(2)} = -\boldsymbol{\lambda}\mathbf{G}^{(2)}$. Since the two-exciton Green's function enters sandwiched between two two-exciton dipole operators, which may be simplified via

$$\boldsymbol{\mu}^{(0)}\,(\mathbf{I}-\boldsymbol{\lambda})\,\mathbf{G}^{(2)}\,(\mathbf{I}-\boldsymbol{\lambda})\,\boldsymbol{\mu}^{(0),\star} = \boldsymbol{\mu}^{(0)}\,(\mathbf{I}-\boldsymbol{\lambda})\,2\mathbf{G}^{(2)}\boldsymbol{\mu}^{(0),\star} = 4\boldsymbol{\mu}^{(0)}\mathbf{G}^{(2)}\boldsymbol{\mu}^{(0),\star}. \quad \text{(E.4)}$$

This factor of 4 will be canceled by the factor of $\frac{1}{4}$ introduced by one of the two-exciton blocks of the identity operator when it is inserted into the above correlation functions (the two-exciton block of the identity is inserted on both sides of $\mathbf{G}^{(2,0)}\boldsymbol{\Gamma}^{(2)}\mathbf{G}^{(2,0)}$). Thus, we may simply replace the dipole moments with their harmonic counterparts in the above expressions for the signals. Note that there are two dipoles accessing the two-exciton manifold, each contributing a factor of $\sqrt{2}$, the result is a factor of 2 for each of the above signals. Since the remaining dipoles and Green's functions are in the single-exciton space, we may evaluate simply by inserting the identity matrix between the operators in the correlation functions above. This requires the evaluation of matrix elements:

$$(\mathbf{G}^{(2,0)}\boldsymbol{\Gamma}^{(2)}\mathbf{G}^{(2,0)})_{12,34} = G^{(2,0)}_{12,1'2'}\Gamma^{(2)}_{1'2',3'4'}G^{(2,0)}_{3'4',34} = \mathcal{G}_{21}(\delta_{2,2'}\delta_{1,1'})\Gamma^{(2)}_{1'2',3'4'}\mathcal{G}_{34}(\delta_{3,3'}\delta_{4,4'}),$$

where we have used equation (B.2). Noticing that $\Gamma^{(2)}_{12,34} = \Gamma^{(2)}_{12,43} = \Gamma^{(2)}_{21,34}$, which follows directly from the definition via Bethe–Salpeter equation and the time reversal symmetry of non-interacting Greens function (i.e. $G^{(2,0)}_{43,4'3'} = G^{(2,0)}_{34,3'4'}$), we can simplify the above equation to

$$(\mathbf{G}^{(2,0)}\boldsymbol{\Gamma}^{(2)}\mathbf{G}^{(2,0)})_{12,34} = 4\mathcal{G}_{12}\Gamma_{12,34}\mathcal{G}_{34}. \quad \text{(E.5)}$$

This cancels the remaining factor of 4 introduced by the insertion of the over-complete identity operators. The time convolutions in the response functions are then evaluated by substituting equation (E.12). Since the result is to be plotted with respect to two of the frequencies conjugate to the time arguments, we will Fourier transform the signals according to

$$P_{\mathrm{I,II}}\,(\Omega_3, t_2, \Omega_1) = \int\int P_{\mathrm{I,II}}\,(t_3, t_2, t_1)\,\mathrm{e}^{\mathrm{i}\Omega_3 t_3}\,\mathrm{e}^{\mathrm{i}\Omega_1 t_1}\,\mathrm{d}t_1\,\mathrm{d}t_3, \quad \text{(E.6)}$$

$$P_{\mathrm{III}}\,(\Omega_3, \Omega_2, t_1) = \int\int P_{\mathrm{III}}\,(t_3, t_2, t_1)\;\mathrm{e}^{\mathrm{i}\Omega_3 t_3}\,\mathrm{e}^{\mathrm{i}\Omega_2 t_2}\,\mathrm{d}t_2\,\mathrm{d}t_3. \quad \text{(E.7)}$$

This is shown in detail in sections E.1 and E.2 and results in equations (44)–(46).

Turning now to the fifth-order diagrams under consideration in section 5 and shown in figure 6, the time-domain response functions are easily read off from the rules in appendices B and C:

$$\begin{aligned} S^{(5)}_{\mathrm{a}}(t_2, t_1) = \theta\,(t_1)\,\theta\,(t_2)\int_0^{t_1}\mathrm{d}\tau'\int_0^{\tau'}\mathrm{d}\tau''\langle\hat{\mu}^-\hat{G}^{(1)}(t_2)\hat{\mu}^-\hat{\mu}^-\hat{G}^{(3,0)}(t_1-\tau')\hat{\Gamma}^{(3)}(\tau'-\tau'') \\ \times\hat{G}^{(3,0)}(\tau'')\hat{\mu}^+\hat{\mu}^+\hat{\mu}^+\rangle, \end{aligned} \quad \text{(E.8)}$$

$$\begin{aligned} S^{(5)}_{\mathrm{b}}(t_2, t_1) = \theta\,(t_1)\,\theta\,(t_2)\int_0^{t_2}\mathrm{d}\tau_2'\int_0^{\tau_2'}\mathrm{d}\tau_2''\int_0^{t_1+t_2}\mathrm{d}\tau'\int_0^{\tau_1'}\mathrm{d}\tau_1''\langle\hat{\mu}^-\hat{\mu}^-\hat{G}^{(2,0),\dagger}(t_2-\tau_2') \\ \times\hat{\Gamma}^{(2),\dagger}(\tau_2'-\tau_2'')\hat{G}^{(2,0),\dagger}(\tau_2'')\hat{\mu}^-\hat{G}^{(3,0)}(t_1+t_2-\tau_1') \\ \times\hat{\Gamma}^{(3)}(\tau_1'-\tau_1'')\hat{G}^{(3,0)}(\tau_1'')\hat{\mu}^+\hat{\mu}^+\hat{\mu}^+\rangle, \end{aligned} \quad \text{(E.9)}$$

$$S_{\mathrm{c}}^{(5)}(t_2,t_1) = -\theta\,(t_1)\,\theta\,(t_2)\int_0^{t_2}\mathrm{d}\tau_2'\int_0^{\tau_2'}\mathrm{d}\tau_2''\int_0^{t_1}\mathrm{d}\tau'\int_0^{\tau_1'}\mathrm{d}\tau_1''\langle\hat{\mu}^-\hat{G}^{(1),\dagger}(t_2)\hat{\mu}^-\hat{G}^{(2,0)}(t_2-\tau_2')$$
$$\times\hat{\Gamma}^{(2),\dagger}(\tau_2'-\tau_2'')\hat{G}^{(2,0),\dagger}(\tau_2'')\hat{\mu}^-\hat{G}^{(3,0)}(t_1-\tau_1')\hat{\Gamma}^{(3)}(\tau_1'-\tau_1'')\hat{G}^{(3,0)}(\tau_1'')\hat{\mu}^+\hat{\mu}^+\hat{\mu}^+\rangle. \tag{E.10}$$

Following the same method as for the third-order signals and evaluating these correlation functions, one inserts the identity given by equation (A.9) between all operators in the above correlation functions. The result is then Fourier transformed with respect to the two time intervals. Once again, the convolutions can be carried out analytically by making the substitution in equation (E.12). These manipulations result in equations (48)–(50).

E.1. Derivation of the $\mathbf{k_I} = -\mathbf{k_1}+\mathbf{k_2}+\mathbf{k_3}$ *signal*

We begin with equation (E.1) (see figure 5) and perform the simplification of the dipole moments to those of single-excitation described above. This crucial simplification for the scattering matrix approach also holds for NEE formalism in [27] thus not being specific for the coboson representation. Expanding equation (E.1) in the coboson basis yields

$$S_{\mathrm{I}}\,(t_3,t_2,t_1) = -2\theta\,(t_1)\,\theta\,(t_2)\,\theta\,(t_3)\sum_{4,\ldots,1}\mu_4\mu_3^*\mu_2^*\mu_1 I_2(t_2)\mathcal{G}_1^{\dagger}(t_1+t_2+t_3)\mathcal{G}_4(t_3)\mathcal{G}_1(t_3)$$
$$\times\int_0^{t_3}\mathrm{d}\tau'\int_0^{\tau'}\mathrm{d}\tau''\mathcal{G}_4(-\tau')\mathcal{G}_1(-\tau')\Gamma_{32,41}(\tau'-\tau'')\mathcal{G}_2(\tau'')\mathcal{G}_3(\tau''). \tag{E.11}$$

In order to carry out the convolution integrals, we Fourier transform the scattering matrix according to

$$\mathbf{\Gamma}^{(2)}(t) = \int\frac{\mathrm{d}\omega}{2\pi}\mathrm{e}^{-\mathrm{i}\omega t}\mathbf{\Gamma}^{(2)}(\omega) \tag{E.12}$$

and explicitly write out the Green's functions as exponentials:

$$S_{\mathrm{I}}\,(t_3,t_2,t_1) = 2\theta\,(t_1)\,\theta\,(t_2)\,\theta\,(t_3)\sum_{4,3,2,1}\mu_4\mu_3^*\mu_2^*\mu_1\,\mathrm{e}^{-\mathrm{i}(\zeta_2-\zeta_1)t_2}\,\mathrm{e}^{\mathrm{i}\zeta_1^* t_1}\,\mathrm{e}^{-\mathrm{i}\zeta_4 t_3}\,\mathrm{e}^{2\mathrm{i}\mathrm{i}\gamma_1 t_3}$$
$$\times\int\mathrm{d}\omega\frac{(i)(-i)(-i)\Gamma_{32,41}(\omega)}{2\pi}\int_0^{t_3}\mathrm{d}\tau'\,\mathrm{e}^{-\mathrm{i}(\omega-\zeta_4-\zeta_1)\tau'}\int_0^{\tau'}\mathrm{d}\tau''\,\mathrm{e}^{\mathrm{i}(\omega-\zeta_2-\zeta_3)\tau''}. \tag{E.13}$$

Since each forward (backward) propagation through time is accompanied by a factor $-\mathrm{i}$ (i), an overall factor of (i)$(-\mathrm{i})(-\mathrm{i})$ is introduced. In the above equation the time depend integrals can be carried out analytically as

$$\int_0^{t_3}\mathrm{d}\tau'\,\mathrm{e}^{-\mathrm{i}(\omega-E_4-E_1)\tau'}\int_0^{\tau'}\mathrm{d}\tau''\,\mathrm{e}^{\mathrm{i}(\omega-E_2-E_3)\tau''} = \int_0^{t_3}\mathrm{d}\tau'\,\mathrm{e}^{-\mathrm{i}(\omega-E_4-E_1)\tau'}\frac{\mathrm{e}^{\mathrm{i}(\omega-E_2-E_3)\tau'}-1}{i(\omega-E_2-E_3)}$$
$$=\frac{1}{\mathrm{i}(\omega-E_2-E_3)}\left[\frac{\mathrm{e}^{\mathrm{i}(E_4+E_1-E_2-E_3)t_3}-1}{\mathrm{i}(E_4+E_1-E_2-E_3)}-\frac{\mathrm{e}^{-\mathrm{i}(\omega-E_4-E_1)t_3}-1}{-\mathrm{i}(\omega-E_4-E_1)}\right]. \tag{E.14}$$

Formally, our next step will be to Fourier transform with respect to t_3 and t_1 via

$$S_{\mathrm{I}}(\Omega_3, t_2, \Omega_1) = \int_0^\infty \mathrm{d}t_3 \int_0^\infty \mathrm{d}t_1\, \mathrm{e}^{\mathrm{i}\Omega_1 t_1}\, \mathrm{e}^{\mathrm{i}\Omega_3 t_3} S_{\mathrm{I}}(t_3, t_2, t_1)\,. \tag{E.15}$$

In anticipation of our subsequent integration over $\mathrm{d}\omega$ by closing the contour in the upper half plane (which will introduce a factor of $2\pi\mathrm{i}$ by the residue theorem), we will drop the first, second and fourth terms in equation (E.14) on the grounds that their poles are all in the lower half plane. The only term which will contribute therefore is

$$S_{\mathrm{I}}(\Omega_3, t_2, \Omega_1) = -2\theta(t_2) \sum_{4,3,2,1} \mu_4 \mu_3^\star \mu_2^\star \mu_1 \frac{\mathrm{e}^{-\mathrm{i}(E_2 - E_1)t_2}}{\Omega_1 - E_1^*}$$

$$\times \int \mathrm{d}\omega \frac{\Gamma_{32,41}(\omega)}{(\omega - E_2 - E_3)(\omega - E_4 - E_1)(\omega - E_1 - 2\mathrm{i}\gamma_1 - \Omega_3)}. \tag{E.16}$$

Note that the residue integral and the Green's functions together introduce a factor of $(\mathrm{i})(\mathrm{i})(-\mathrm{i})(-\mathrm{i})$ to the numerator of the above expression while the integrals over τ', τ'' each introduce a factor of i to the denominator and the integrals over t_1, t_3 each introduce a factor of $-\mathrm{i}$ to the denominator. Thus, all these imaginary factors cancel and we are left with equation (E.16). There is a lone pole in the upper half plane at $\omega = E_1 + 2\mathrm{i}\gamma_1 + \Omega_3$ (see figure 11(B)). The origin of this pole is the factor of $\mathrm{e}^{2i\gamma_1 t_3}$ introduced by the product $\mathcal{G}_1^\dagger(t_3) \times \mathcal{G}_1(t_3)$. We may thus carry out the $\mathrm{d}\omega$ integration, arriving at

$$S_{\mathrm{I}}(\Omega_3, t_2, \Omega_1) = -2\theta(t_2) \sum_{4,3,2,1} \mu_4 \mu_3^\star \mu_2^\star \mu_1 \frac{\mathrm{e}^{-\mathrm{i}(E_2 - E_1)t_2}}{\Omega_1 - E_1^\star} \frac{\Gamma_{32,41}(E_1 + \mathrm{i}\gamma_1 + \Omega_3)}{(E_1 + \mathrm{i}\gamma_1 + \Omega_3 - E_2 - E_3)(\Omega_3 - E_4 + 2\mathrm{i}\gamma_1)}$$

$$= -2\theta(t_2) \sum_{4,3,2,1} \mu_4 \mu_3^\star \mu_2^\star \mu_1 \mathcal{G}_1^\star(-\Omega_1)\, \mathcal{G}_1^\star(t_2)\, \mathcal{G}_2(t_2)\, \mathcal{G}_4(\Omega_3 + 2\mathrm{i}\gamma_1)$$

$$\times \Gamma_{32,41}^{(2)}(\Omega_3 + E_1 + \mathrm{i}\gamma_1)\, \mathcal{G}_{32}(\Omega_3 + E_1 + \mathrm{i}\gamma_1)\,. \tag{E.17}$$

Because the signal is related to the polarization by equation (42), we may obtain $P_{\mathrm{I}}(\Omega_3, t_2, \Omega_1)$ from $S_{\mathrm{I}}(\Omega_3, t_2, \Omega_1)$ by transforming $\Omega_1 \to \Omega_1 - \omega_1$, $\Omega_3 \to \Omega_3 - \omega_1 + \omega_2 + \omega_3$. This immediately gives equations (44)–(46) are obtained similarly.

E.2. Derivation of $\mathbf{k}_{\mathrm{III}} = \mathbf{k}_1 + \mathbf{k}_2 - \mathbf{k}_3$ *signal*

Due to cancellation of the diagrams in figure 12 ($\mathrm{III}_{\mathrm{a}0}$ cancels out $\mathrm{III}_{\mathrm{b}0}$ and $\mathrm{III}_{\mathrm{a}1}$ cancels out $\mathrm{III}_{\mathrm{b}1}$) we obtain the signal in the time domain

$$S_{\mathrm{III}}^{(3)}(t_3, t_2, t_1) = S_{b1,2}^{(3)}(t_3, t_2, t_1)$$

$$= -\theta(t_3)\theta(t_2)\theta(t_1) \int_{t_2}^{t_2+t_3} \mathrm{d}\tau' \int_0^{\tau'} \mathrm{d}\tau'' \langle \hat{\mu}^- \hat{G}^\dagger(t_3) \hat{\mu}^- \hat{G}^{(0,2)}(t_2 + t_3 - \tau') \hat{\Gamma}^{(2)}(\tau' - \tau'')$$

$$\times \hat{G}^{(0,2)}(\tau'') \hat{\mu}^+ \hat{G}(t_1) \hat{\mu}^+ \rangle. \tag{E.18}$$

This form of the expression is basis independent. At this point, we introduce the coboson algebra by inserting the identity operator in equation (E.9) and, using equations ((E.4), B10, (36), (37)), we obtain the signal in coboson representation:

$$
\begin{aligned}
&S^{(3)}_{\mathrm{III}}(t_3,t_2,t_1)\\
&= -2\theta(t_3)\theta(t_2)\theta(t_1)\sum_{1,2,3,4}\mu_4\mu_3\mu_2^{\star}\mu_1^{\star}\mathcal{G}_4^{\star}(t_3)\\
&\qquad\times\int_{t_2}^{t_2+t_3}\mathrm{d}\tau'\int_0^{\tau'}\mathrm{d}\tau''\mathcal{G}_{43}(t_2+t_3-\tau')\Gamma^{(2)}_{43,21}(\tau'-\tau'')\mathcal{G}_{21}(\tau'')\mathcal{G}_1(t_1)\\
&= -i2\theta(t_3)\theta(t_2)\theta(t_1)\sum_{1,2,3,4}\mu_4\mu_3\mu_2^{\star}\mu_1^{\star}\mathcal{G}_4^{\star}(t_3)\mathcal{G}_{43}(t_2+t_3)\mathcal{G}_1(t_1)\\
&\qquad\times\int_{t_2}^{t_2+t_3}\mathrm{d}\tau'\int_0^{\tau'}\mathrm{d}\tau''\mathcal{G}_{43}(-\tau')\Gamma_{43,21}(\tau'-\tau'')\mathcal{G}_{21}(\tau'').
\end{aligned}
\tag{E.19}
$$

In the above expression we have used the fact that $\mathcal{G}_{43}(t_3+t_2-\tau')=\mathrm{i}\mathcal{G}_{43}(t_2+t_3)\mathcal{G}_{43}(-\tau')$.

Transforming the scattering matrix to the frequency domain equation (E.12) we can rewrite the double integral as a triple one

$$
\begin{aligned}
&\int_{t_2}^{t_2+t_3}\mathrm{d}\tau'\int_0^{\tau'}\mathrm{d}\tau''\mathcal{G}_{43}(-\tau')\Gamma^{(2)}_{43,21}(\tau'-\tau'')\mathcal{G}_{21}(\tau'')=\frac{1}{2\pi}\int\mathrm{d}\omega\Gamma^{(2)}_{43,21}(\omega)\\
&\qquad\times\int_{t_2}^{t_2+t_3}\mathrm{d}\tau'\mathcal{G}_{43}(-\tau')\mathrm{e}^{-\mathrm{i}\omega\tau'}\int_0^{\tau'}\mathrm{d}\tau''\mathcal{G}_{21}(\tau'')\mathrm{e}^{\mathrm{i}\omega\tau''}.
\end{aligned}
\tag{E.20}
$$

The inner double integral can be represented as

$$
\int_{t_2}^{t_2+t_3}\mathrm{d}\tau'\mathcal{G}_{43}(-\tau')\mathrm{e}^{-\mathrm{i}\omega\tau'}\int_0^{\tau'}\mathrm{d}\tau''\mathcal{G}_{21}(\tau'')\mathrm{e}^{\mathrm{i}\omega\tau''}=\mathcal{G}_{21}(\omega)[I1(t_2+t_3)-I1(t_2)+I2(t_2+t_3)-I2(t_2)],
\tag{E.21}
$$

where we have introduced

$$
I1(t)=\frac{\mathrm{e}^{\mathrm{i}t(E_3+E_4-\omega)}}{\omega-E_3-E_4},
\tag{E.22}
$$

$$
I2(t)=\frac{\mathrm{e}^{-\mathrm{i}t(E_1+E_2-E_3-E_4)}}{E_3+E_4-E_1-E_2}.
\tag{E.23}
$$

Since both $\Gamma_{43,21}(\omega)$ and $I2$ have poles in the lower half plane, it is convenient to chose the integration contour on ω in the *upper* half-plane (figure 11). This makes $I2$ terms in equation (E.21) disappear.

Now, let us take the Fourier transform with respect to t_2, t_3:

$$S^{(3)}_{\mathrm{III}}(\Omega_3,\Omega_2,t_1)=\int \mathrm{d}t_3\,\mathrm{e}^{\mathrm{i}\Omega_3 t_3}\int \mathrm{d}t_2\,\mathrm{e}^{\mathrm{i}\Omega_2 t_2}S^{(3)}_{\mathrm{III}}(t_3,t_2,t_1)$$

$$=\mathrm{i}\theta(t_1)\sum_{1,2,3,4}\mu_4\mu_3\mu_2^{\star}\mu_1^{\star}\mathcal{G}_1(t_1)\int\frac{\mathrm{d}\omega}{2\pi}\mathcal{G}_{43}(\omega)\Gamma^{(2)}_{43,21}(\omega)I_{21}(\omega)$$

$$\left[\frac{1}{\omega-\Omega_2}\frac{1}{\omega-\Omega_3-(E_4-\mathrm{i}\gamma_4)}+\frac{1}{\omega-\Omega_2}\frac{1}{\Omega_3-(E_3-\mathrm{i}\gamma_3)}\right]. \tag{E.24}$$

The above integral was calculated via the integration contour as shown in figure 11(A). That is, the flat portion of the integration contour is tracing the lower boundary of the imaginary part of the two-particle excitation region and then closes in the upper half-plane. Finally, by applying the residue theorem and replacing $\Omega_1\to\Omega_1+\omega_1$, $\Omega_2\to\Omega_2+\omega_1+\omega_2$, $\Omega_3\to\Omega_3+\omega_1+\omega_2-\omega_3$ to account for the field carrier frequency (equation (42)), we obtain

$$P^{(3)}_{\mathrm{III}}(\Omega_3,\Omega_2,t_1)=-2\theta(t_1)\sum_{4,\ldots,1}\mu_4\mu_3\mu_2^{\star}\mu_1^{\star}\mathcal{G}_1(t_1)[\mathcal{G}_{43}(\Omega_2+\omega_1+\omega_2)\,\Gamma^{(2)}_{43,21}(\Omega_2+\omega_1+\omega_2)$$

$$\times\mathcal{G}_{21}(\Omega_2+\omega_1+\omega_2)\,\mathcal{G}_4(\Omega_2-\Omega_3+\omega_3)$$

$$-\mathcal{G}_{43}(\Omega_3+\omega_1+\omega_2-\omega_3+E_4)\,\Gamma^{(2)}_{43,21}$$

$$\times(\Omega_3+\omega_1+\omega_2-\omega_3+E_4)\,\mathcal{G}_{21}(\Omega_3+\omega_1+\omega_2-\omega_3+E_4)$$

$$\times\mathcal{G}_4(\Omega_2-\Omega_3+\omega_3)+\mathcal{G}_{43}(\Omega_2+\omega_1+\omega_2)\,\Gamma^{(2)}_{43,21}(\Omega_2+\omega_1+\omega_2)$$

$$\times\mathcal{G}_{21}(\Omega_2+\omega_1+\omega_2)\,\mathcal{G}_3(\Omega_3+\omega_1+\omega_2-\omega_3)]. \tag{E.25}$$

We can simplify equation (E.25) a bit further by noticing that

$$\mathcal{G}_{43}(\Omega_3+\omega_1+\omega_2-\omega_3+E_4)=\mathcal{G}_3(\Omega_3+\omega_1+\omega_2-\omega_3)\,,$$

$$\mathcal{G}_{43}(\Omega_2+\omega_1+\omega_2)\,(\mathcal{G}_4(\Omega_2-\Omega_3+\omega_3)+\mathcal{G}_3(\Omega_3+\omega_1+\omega_2-\omega_3))$$

$$=\mathcal{G}_4(\Omega_2-\Omega_3+\omega_3)\,\mathcal{G}_3(\Omega_3+\omega_1+\omega_2-\omega_3)\,, \tag{E.26}$$

so that we are left with two terms only as in equation (46).

Note that, in equation (E.24), we could bring the poles in the first term to the upper half-plane by simply changing the variable $E_4\to E_4+2\mathrm{i}\gamma_4$ as shown in figure 11(B). This would make the signal in the form

$$P^{(3)}_{\mathrm{III}}(\Omega_3,\Omega_2,t_1)=-2\theta(t_1)\sum_{4,\ldots,1}\mu_4\mu_3\mu_2^{\star}\mu_1^{\star}\mathcal{G}_1(t_1)I_3(\Omega_3+\omega_1+\omega_2-\omega_3)\,\mathcal{G}_4^{\star}(\Omega_2-\Omega_3+\omega_3)$$

$$\times[\Gamma^{(2)}_{43,21}(\Omega_2+\omega_1+\omega_2)\,\mathcal{G}_{21}(\Omega_2+\omega_1+\omega_2)-\Gamma^{(2)}_{43,21}(\Omega_3+\omega_1+\omega_2-\omega_3+E_4+\mathrm{i}\gamma_4)$$

$$\times\mathcal{G}_{21}(\Omega_3+\omega_1+\omega_2-\omega_3+E_4+\mathrm{i}\gamma_4)]. \tag{E.27}$$

This form coincides with [18].

Appendix F. Sum-over-states expressions for the third-order impulsive response

$$P_{\mathrm{I}}^{(\mathrm{SOS})}(\Omega_3, t_2, \Omega_1) = \mathrm{i}\sum_{e_2,e_1} \mu_{g,e_1}\mu^*_{g,e_1}\mu^*_{g,e_2}\mu_{g,e_2}\mathcal{G}^*_{e_2}(-\Omega_1+\omega_1)\mathcal{G}^*_g(t_2)I_g(t_2)\mathcal{G}_{e_1}(\Omega_3-\omega_1+\omega_2+\omega_3)$$
$$+\mathrm{i}\sum_{e_2,e_1} \mu_{g,e_1}\mu^*_{g,e_2}\mu^*_{g,e_1}\mu_{g,e_2}\mathcal{G}^*_{e_2}(-\Omega_1+\omega_1)\mathcal{G}^*_{e_2}(t_2)I_{e_1}(t_2)\mathcal{G}_{e_1}(\Omega_3-\omega_1+\omega_2+\omega_3)$$
$$-\mathrm{i}\sum_{e_2,e_1,f} \mu_{e_2,f}\mu^*_{e_1,f}\mu^*_{g,e_1}\mu_{g,e_2}\mathcal{G}^*_{e_1}(-\Omega_1+\omega_1)\mathcal{G}^*_{e_2}(t_2)\mathcal{G}_{e_2}(t_2)\mathcal{G}_{fe_2}(\Omega_3-\omega_1+\omega_2+\omega_3), \tag{F.1}$$

$$P_{\mathrm{II}}^{(\mathrm{SOS})}(\Omega_3, t_2, \Omega_1) = -\mathrm{i}\sum_{e_2,e_1} \mu^*_{g,e_2}\mu_{g,e_2}\mu_{g,e_1}\mu^*_{g,e_1}\mathcal{G}_{e_1}(\Omega_1+\omega_1)\mathcal{G}^*_g(t_2)\mathcal{G}_g(t_2)\mathcal{G}_{e_2}(\Omega_3+\omega_1-\omega_2+\omega_3)$$
$$-\mathrm{i}\sum_{e_2,e_1} \mu_{g,e_1}\mu^*_{g,e_2}\mu_{g,e_2}\mu^*_{g,e_1}\mathcal{G}_{e_1}(\Omega_1+\omega_1)\mathcal{G}^*_{e_2}(t_2)\mathcal{G}_{e_1}(t_2)\mathcal{G}_{e_1}(\Omega_3+\omega_1-\omega_2+\omega_3)$$
$$+\mathrm{i}\sum_{e_2,e_1,f} \mu_{e_2,f}\mu^*_{e_1,f}\mu_{g,e_2}\mu^*_{g,e_1}\mathcal{G}_{e_1}(\Omega_1+\omega_1)\mathcal{G}^*_{e_2}(t_2)\mathcal{G}_{e_1}(t_2)\mathcal{G}_{fe_2}(\Omega_3+\omega_1-\omega_2+\omega_3), \tag{F.2}$$

$$P_{\mathrm{III}}^{(\mathrm{SOS})}(\Omega_3, \Omega_2, t_1) = -\mathrm{i}\sum_{e_2,e_1,f} \mu_{g,e_1}\mu_{e_1,f}\mu^*_{e_2,f}\mu^*_{g,e_2}\mathcal{G}_{e_2}(t_1)\mathcal{G}_f(\Omega_2+\omega_1+\omega_2)\mathcal{G}_{e_1}(\Omega_3+\omega_1+\omega_2-\omega_3)$$
$$+\mathrm{i}\sum_{e_2,e_1,f} \mu_{g,e_1}\mu_{e_1,f}\mu^*_{e_2,f}\mu^*_{g,e_2}\mathcal{G}_{e_2}(t_1)\mathcal{G}_f(\Omega_2+\omega_1+\omega_2)\mathcal{G}_{fe_1}(\Omega_3+\omega_1+\omega_2-\omega_3), \tag{F.3}$$

where $\mathcal{G}_e = \mathcal{G}_1$ and $\mathcal{G}_{f,e} = 1/(\omega - E_f + E_e + \mathrm{i}\gamma)$. These expressions are easily read off the corresponding diagrams in figures 3 and 4. Note that the states e_i in the SOS formula are equivalent to the states i from the quasiparticle expressions since they were obtained in either case from diagonalization of the one-exciton manifold. Here, we use the notation e_1 for these states to reinforce that the expressions are in the SOS picture. Unlike in the quasiparticle picture, implementing the SOS expressions requires diagonalizing the second exciton manifold in order to obtain the two-exciton energies $\{E_f\}$. The major effort is now shifted to computing the energies $\{E_f\}$. Once these are known, the expressions for the nonlinear response are very simple. In the coboson representation, those are given by diagonalization of the n-exciton block. The single-exciton block (diagonalized in exciton basis $|1\rangle$) as well as two- and three-exciton blocks are

$$H^{(1)}_{1;2} = \delta_{1,2}E_1, \tag{F.4}$$

$$\|\tilde{\boldsymbol{\lambda}}^{(2)}\|\, H^{(2)}_{12;34} = (E_2+E_1)\,\tilde{\lambda}^{(2)}_{12;34} + \sum_{3'4'} \xi_{21;4'3'}\tilde{\lambda}^{(2)}_{3'4';34}, \tag{F.5}$$

$$\|\tilde{\boldsymbol{\lambda}}^{(3)}\| H^{(3)}_{123;456} = (E_1+E_2+E_3)\,\tilde{\lambda}^{(3)}_{3'4'2;456} + \sum_{3',4'}\left(\xi_{21;4'3'}\tilde{\lambda}^{(3)}_{3'4'3;456} + \xi_{31;4'3'}\tilde{\lambda}^{(3)}_{3'4'2;456} + \xi_{32;4'3'}\tilde{\lambda}^{(3)}_{13'4';456}\right), \tag{F.6}$$

where $\tilde{\boldsymbol{\lambda}}^{(n)} = \boldsymbol{\Delta}^{(n)} - \boldsymbol{\Lambda}^{(n)}$ and $\|\tilde{\boldsymbol{\lambda}}^{(n)}\|$ is the norm of the matrix defined in a regular way as the maximum of its singular values. The above blocks can be written in a compact matrix notation as

$$\|\tilde{\boldsymbol{\lambda}}^{(n)}\|\mathbf{H}^{(n)} = \left[\left(\mathbf{G}^{(n,0)}(\omega=0)\right)^{-1} + \boldsymbol{\Xi}^{(n)}\right]\tilde{\boldsymbol{\lambda}}^{(n)}.$$

Although it seems straightforward to obtain the two and three exciton energies by diagonalizing corresponding Hamiltonian blocks, there are some subtleties to the procedure. Based on the fact that $\tilde{\boldsymbol{\lambda}}^{(n)}\tilde{\boldsymbol{\lambda}}^{(n)} = \tilde{\boldsymbol{\lambda}}^{(n)}$ it is tempting to refer to it as the projector on the true physical two-exciton space. However the matrix turns out to be singular due to the over-completeness of the coboson basis. Therefore, as a first step, we can make its Schur decomposition via a unitary matrix $\mathbf{Q}^{(n)}$ so that the transformed Hamiltonian block become

$$\|\tilde{\boldsymbol{\lambda}}^{(n)}\|\tilde{\mathbf{H}}^{(n)} = \mathbf{Q}^{(n)}\left[\left(\mathbf{G}^{(n,0)}(\omega=0)\right)^{-1} + \boldsymbol{\Xi}^{(n)}\right](\mathbf{Q}^{(n)})^{-1}\mathbf{Q}^{(n)}\tilde{\boldsymbol{\lambda}}^{(n)}(\mathbf{Q}^{(n)})^{-1}.$$

Although Schur decomposition guarantees an upper triangular matrix, the decomposed $\mathbf{Q}^{(n)}\tilde{\boldsymbol{\lambda}}^{(n)}(\mathbf{Q}^{(n)})^{-1}$ matrix happen to be almost diagonal and all off-diagonal elements can be safely neglected. There are few nonzero unitary entries on the diagonal. The number of those entries correspond to the physical space of two-exciton manifold sized as $N(N-1)/2$. The resulting Hamiltonian $\tilde{\mathbf{H}}^{(n)}$ becomes block-diagonal with the lower block made of zeros. The upper block can be SVD decomposed. For two-exciton manifold, the decomposition can be written as

$$\tilde{\mathbf{H}}^{(2)} = \tilde{\mathbf{U}}\mathbf{H}^{(2)}_{\mathrm{diag}}\tilde{\mathbf{V}}, \tag{F.7}$$

where $\mathbf{H}^{(2)}_{\mathrm{diag}}$ is the diagonal matrix whose non-zero elements are members of E_f manifold. The zero energy entries due to the lower block can be neglected since they are off-resonant and not physical. There's a small numerical error associated with SVD algorithms, however we need such decomposition since the upper (non-zero) block of $\mathbf{H}^{(2)}_{\mathrm{diag}}$ is still weakly singular. In order to overcome this error, one can project $\mathbf{H}^{(n)}$ back on the on-site basis

$$H^{(2)}_{mn,m'n'} = \frac{1}{(2!)^4}\sum_{4,\ldots,1}\langle m1n1\,m2n2l|12\rangle\langle 12|H^{(2)}|34\rangle\langle 34|m1'n1'm2'n2'\rangle,$$

where we have used the identity operator in the overcomplete basis (appendix A). In order to avoid the nonphysical states, we demand the ordering of the composite indices be $m > n, m' > n'$, so that the projecting matrix $\langle 34|m1'n1'm2'n2'\rangle$ becomes rectangular of size $N^2 \times N(N-1)/2$. After some algebra, we can obtain the projected matrix in the analytical form:

$$\begin{aligned}
&H^{(2)}_{mn,m'n'}\\
&= \left(t^{(1)}_{m1,m1'}\delta_{n1,n1'} + t^{(1)}_{m1,n1'}\delta_{n1,m1'} + t^{(1)}_{n1,m1'}\delta_{m1,n1'} + t^{(1)}_{n1,n1'}\delta_{m1,m1'}\right)\delta_{m2,m2'}\delta_{n2,n2'}\\
&+ \left(t^{(1)}_{m2,m2'}\delta_{n2,n2'} + t^{(1)}_{m2,n2'}\delta_{n2,m2'} + t^{(1)}_{n2,m2'}\delta_{m2,n2'} + t^{(1)}_{n2,n2'}\delta_{m2,m2'}\right)\delta_{m1,m1'}\delta_{n1,n1'}\\
&+ \left(V^{(1)}_{m1,n1} + V^{(2)}_{m2,n2} - W^{(1,2)}_{m1,m2} - W^{(1,2)}_{m1,n2} - W^{(1,2)}_{n1,m2} - W^{(1,2)}_{n1,n2}\right)\delta_{m1,m1'}\delta_{n1,n1'}\delta_{m2,m2'}\delta_{n2,n2'}
\end{aligned}$$

$$+\left(W^{(1,2)}_{m1,m1'}\delta_{n1,n1'}(\delta_{m1,m2}\delta_{n2,n2'}+\delta_{m1,n2}\delta_{m2,n2'})+W^{(1,2)}_{n1,m1'}\delta_{m1,n1'}(\delta_{n1,m2}\delta_{n2,n2'}+\delta_{n1,n2}\delta_{m2,n2'})\right)\delta_{m1',m2'}$$

$$+\left(W^{(1,2)}_{m1,m1'}\delta_{n1,n1'}(\delta_{m1,m2}\delta_{n2,m2'}+\delta_{m1,n2}\delta_{m2,m2'})+W^{(1,2)}_{n1,m1'}\delta_{m1,n1'}(\delta_{n1,m2}\delta_{n2,m2'}+\delta_{n1,n2}\delta_{m2,m2'})\right)\delta_{m1',n2'}$$

$$+\left(W^{(1,2)}_{m1,n1'}\delta_{n1,m1'}(\delta_{m1,m2}\delta_{n2,n2'}+\delta_{m1,n2}\delta_{m2,n2'})+W^{(1,2)}_{n1,n1'}\delta_{m1,m1'}(\delta_{n1,m2}\delta_{n2,n2'}+\delta_{n1,n2}\delta_{m2,n2'})\right)\delta_{n1',m2'}$$

$$+\left(W^{(1,2)}_{m1,n1'}\delta_{n1,m1'}(\delta_{m1,m2}\delta_{n2,m2'}+\delta_{m1,n2}\delta_{m2,m2'})+W^{(1,2)}_{n1,n1'}\delta_{m1,m1'}(\delta_{n1,m2}\delta_{n2,m2'}+\delta_{n1,n2}\delta_{m2,m2'})\right)\delta_{n1',n2'},$$

where the numerical parameters of the above Hamiltonian block are given in the main text.

In order to obtain the nonlinear third-order response functions, we also need to know the dipole moments between the ground state and the single-exciton manifold as well as from the single- to double-exciton manifold. The single-exciton dipole moment can be readily obtained from equation (20)

$$\mu^\star_e = \langle g|B_1 \sum_2 \mu^\star_2 B^\dagger_2|g\rangle = \mu^\star_1. \tag{F.8}$$

The matrix elements from the singly to the doubly excited manifold are similarly obtained from equations (20) and (B.3):

$$\mu^\star_{43,1} = \langle g|B_4 B_3 \sum_2 \mu^\star_2 B^\dagger_2 B^\dagger_1|g\rangle = \sum_2 \mu^\star_2 \tilde{\lambda}^{(2)}_{12,34}. \tag{F.9}$$

Note that, from above expression, we obtain the well known relation $\mu^\star_{11,1} = 2\mu^\star_1$ for a harmonic oscillator. The SVD decomposition of the two-exciton block in equation (F.7) provides the dipole moments between the two- and single-exciton manifolds

$$\mu^\star_{f,e} = \sum_2 \mu^\star_2 \sum_{1',2',3',4'} \tilde{U}_{43,4'3'}\tilde{\lambda}^{(2)}_{4'3',2'1'}\tilde{V}_{2'1',21}. \tag{F.10}$$

In the above equation, the two-exciton matrices $\tilde{\mathbf{U}}$ and $\tilde{\mathbf{V}}$ must be augmented with the zero block in order to match the size of the coboson based matrix $\tilde{\boldsymbol{\lambda}}^{(n)}$. The procedure assigns some small dipole elements to the unphysical states, but due to their off-resonant nature, this does not affect the final signals.

Appendix G. Third-order signals with exciton transport

The effects of coupling to a bath can be incorporated to the above signals easily by averaging the product of Green's functions for each time interval. Assuming the bath does not couple separate exciton manifolds, this averaging need only be carried out for time periods during which the density matrix is in the single-exciton manifold. As can be seen by the diagrams, only the $\mathbf{k}_{\mathrm{I}}$ and $\mathbf{k}_{\mathrm{II}}$ techniques go through excited state populations and so only these third-order techniques will be affected. The result of this bath coupling is that the exciton states will now change during the time-period in question. This is known as exciton transport. The resulting signals for the $\mathbf{k}_{\mathrm{I}}$ and $\mathbf{k}_{\mathrm{II}}$ techniques are

$$\begin{aligned}\bar{P}_{\mathrm{I}}(\Omega_3, t_2, \Omega_1) = -2\theta(t_2) \sum_{4,3,2,1,2',1'} & \mu_4\mu^*_3\mu^*_2\mu_1\mathcal{G}^*_1(-\Omega_1+\omega_1)\,\bar{G}_{2'1',21}(t_2)\mathcal{G}_{32'}(\Omega_3-\omega_1+\omega_2 \\ & +\omega_3+E_{1'}+\mathrm{i}\gamma_{1'})\Gamma^{(2)}_{32',41'}(\Omega_3-\omega_1+\omega_2+\omega_3+E_{1'}+\mathrm{i}\gamma_{1'}) \\ & \times\mathcal{G}_{1'4}(\Omega_3-\omega_1+\omega_2+\omega_3+E_{1'}+\mathrm{i}\gamma_{1'}),\end{aligned} \tag{G.1}$$

$$\bar{P}_{\mathrm{II}}(\Omega_3, t_2, \Omega_1) = -2\theta(t_2) \sum_{4,3,2,1,2',1'} \mu_4\mu_3^*\mu_2\mu_1^* \bar{G}_{1'2',12}(t_2)\mathcal{G}_1(\Omega_1+\omega_1)\,\mathcal{G}_{31'}(\Omega_3+\omega_1-\omega_2$$
$$+\omega_3+E_{2'}+\mathrm{i}\gamma_{2'})\Gamma^{(2)}_{31',42'}(\Omega_3+\omega_1-\omega_2+\omega_3+E_{2'}+\mathrm{i}\gamma_{2'})$$
$$\times\mathcal{G}_{2'4}(\Omega_3+\omega_1-\omega_2+\omega_3+E_{2'}+\mathrm{i}\gamma_{2'})\,. \tag{G.2}$$

Here, we have defined the bath-average Green's function

$$\bar{G}_{12,34} \equiv \langle B_1(t)B_3^\dagger(0)\rho B_2(0)B_4^\dagger(t)\rangle = \langle B_2(0)B_4^\dagger(t)B_1(t)B_3^\dagger(0)\rangle. \tag{G.3}$$

This can be interpreted as a miniature loop progression within the larger loop (see figure 7). In this interpretation, we evolve the ket forward in time from state 3 to state 1 and then evolve the bra backwards from 4 to 2. The tetradic Green's function (equation (G.3)) in excitonic basis represents both coherence and population relaxations. These are decoupled in the Redfield approximation. That is, in between the interaction with the light pulses, the system evolves as

$$\rho_{12}(t) = \sum_{3,4} \tilde{G}_{12;34}(t)\rho_{34}(0), \tag{G.4}$$

where

$$\tilde{G}_{12;34}(t) = \delta_{4,3}\delta_{2,1}\theta(t)\left[\exp(-Kt)\right]_{22;44} + \left(1-\delta_{4,3}\right)\delta_{4,2}\delta_{3,1}\theta(t)\exp\left[-\mathrm{i}(E_4-e_3)t - K_{12;12}t\right].$$

Here $K_{22;44}$ is the population transfer rate (governs the diagonal elements in equation (G.4)) and $K_{12;12}$ is the pure dephasing rate (governs off-diagonal elements in equation (G.4)). A closed form of the K matrix in the eigenstate coboson representation in terms of the harmonic bath spectral density is given in [37].

References

[1] Basov D N, Averitt R D, van der Marel D, Dressel M and Haule K 2011 *Rev. Mod. Phys.* **83** 471
[2] Abrikosov A, Gorkov L and Dzyaloshinski I 1975 *Methods of Quantum Field Theory in Statistical Physics* (Mineola, NY: Dover)
[3] Rammer J 2007 *Quantum Field Theory of Non-Equilibrium States* (Cambridge: Cambridge University Press)
[4] Mahan G D 2011 *Condensed Matter in a Nutshell* (Princeton, NJ: Princeton University Press)
[5] Haug H and Koch S W 1993 *Quantum Theory of Optical and Electronic Properties of Semiconductors* (Singapore: World Scientific)
[6] Bolton S R, Neukirch U, Sham L J, Chemla D S and Axt V M 2000 *Phys. Rev. Lett.* **85** 2002
[7] Karaiskaj D, Bristow A D, Yang L, Dai X, Mirin R P, Mukamel S and Cundiff S T 2010 *Phys. Rev. Lett.* **104** 117401
[8] Turner D B, Wen P, Arias D H and Nelson K A 2011 *Phys. Rev.* B **84** 165321
[9] Oestreich T 2001 *Phys. Rev.* B **64** 245203
[10] Turner D B and Nelson K A 2010 *Nature Lett.* **466** 1089
[11] Scholes G and Rumbles G 2006 *Nature Mater.* **5** 683
[12] Stone K, Gundogdu K, Turner D, Li X, Cundiff S and Nelson K 2009 *Science* **324** 1169
[13] Orenstein J 2012 *Phys. Today* **65** 44
[14] Combescot M, Betbeder-Matibet O and Dubin F 2008 *Phys. Rep.* **463** 215
[15] Hanamura E and Haug H 1977 *Phys. Rep.* **33** 209
[16] Schmitt-Rink S, Ell C and Haug H 1986 *Phys. Rev.* B **33** 1183
[17] Liu Y, Sun C, Yu S and Zhou D 2001 *Phys. Rev.* A **63** 023802

[18] Mukamel S, Oszwaldowski R and Abramavicius D 2007 *Phys. Rev.* B **75** 245305
[19] Chernyak V and Mukamel S 1996 *J. Opt. Soc. Am.* B **13** 1302
[20] Juzeliūnas G and Knoester J 2000 *J. Chem. Phys.* **112** 2325
[21] Combescot M and Betbeder-Matibet O 2004 *Phys. Rev. Lett.* **93** 16403
[22] Combescot M and Betbeder-Matibet O 2008 *Phys. Rev.* B **78** 125206
[23] Petrov D S, Salomon C and Shlyapnikov G V 2005 *J. Phys. B: Atom. Mol. Opt. Phys.* **38** S645
[24] Chesnut D B and Suna A 1963 *J. Chem. Phys.* **39** 146
[25] Haug H and Koch S 2004 *Quantum Theory of the Optical and Electronic Properties of Semiconductors* (Singapore: World Scientific)
[26] Spano F C and Mukamel S 1989 *Phys. Rev.* A **40** 5783
[27] Chernyak V, Zhang W M and Mukamel S 1998 *J. Chem. Phys.* **109** 9587
[28] Abramavicius D and Mukamel S 2010 *J. Chem. Phys.* **133** 184501
[29] Axt V M and Mukamel S 1998 *Rev. Mod. Phys.* **70** 145
[30] Onida G, Reining L and Rubio A 2002 *Rev. Mod. Phys.* **74** 601
[31] Tretiak S and Mukamel S 2002 *Chem. Rev.* **102** 3171
[32] Blaizot J and Ripka G 1986 *Quantum Theory of Finite Systems* (Cambridge, MA: MIT)
[33] Gross E, Dobson J and Petersilka M 1996 *Density Functional Theory* vol 181 (Berlin: Springer)
[34] Casida M 1995 *Recent Advances in Density-Functional Methods* vol 3 (Singapore: World Scientific)
[35] Vinson J, Rehr J J, Kas J J and Shirley E L 2011 *Phys. Rev.* B **83** 115106
[36] Combescot M, Betbeder-Matibet O and Dubin F 2006 *Eur. Phys. J.* B **52** 181
[37] Abramavicius D, Palmieri B, Voronine D V, Sanda F and Mukamel S 2009 *Chem. Rev.* **109** 2350